SPECIAL
GDIS Drought Worldwide
COLLECTION

Did Climate Change–Induced Rainfall Trends Contribute to the Australian Millennium Drought?

WENJU CAI, ARIAAN PURICH, TIM COWAN, PETER VAN RENSCH, AND EVAN WELLER

CSIRO Marine and Atmospheric Research, Aspendale, Victoria, Australia

(Manuscript received 14 June 2013, in final form 6 January 2014)

ABSTRACT

The Australian decade-long "Millennium Drought" broke in the summer of 2010/11 and was considered the most severe drought since instrumental records began in the 1900s. A crucial question is whether climate change played a role in inducing the rainfall deficit. The climate modes in question include the Indian Ocean dipole (IOD), affecting southern Australia in winter and spring; the southern annular mode (SAM) with an opposing influence on southern Australia in winter to that in spring; and El Niño–Southern Oscillation, affecting northern and eastern Australia in most seasons and southeastern Australia in spring through its coherence with the IOD. Furthermore, the poleward edge of the Southern Hemisphere Hadley cell, which indicates the position of the subtropical dry zone, has possible implications for recent rainfall declines in autumn. Using observations and simulations from phase 5 of the Coupled Model Intercomparison Project (CMIP5), it is shown that the drought over southwest Western Australia is partly attributable to a long-term upward SAM trend, which contributed to half of the winter rainfall reduction in this region. For southeast Australia, models simulate weak trends in the pertinent climate modes. In particular, they severely underestimate the observed poleward expansion of the subtropical dry zone and associated impacts. Thus, although climate models generally suggest that Australia's Millennium Drought was mostly due to multidecadal variability, some late-twentieth-century changes in climate modes that influence regional rainfall are partially attributable to anthropogenic greenhouse warming.

1. Introduction

Australia is one of the driest inhabited continents in the world, with a climate that is highly variable and which experiences seasonal-scale droughts with large interdecadal variability (Gallant et al. 2007). Australia is also influenced by several modes of seasonal-scale variability such as the Indian Ocean dipole (IOD), the southern annular mode (SAM), and El Niño–Southern Oscillation (ENSO; e.g., Nicholls et al. 1996; Ashok et al. 2003; Hendon et al. 2007; Risbey et al. 2009; Ummenhofer et al. 2011; and references therein). The influence of these three dominant modes on Australia's climate varies both regionally and seasonally. During the period between the mid-1990s and late 2000s, many Australian regions were plagued by concurrent severe droughts, which later became known as the Millennium Drought (e.g., Ummenhofer et al. 2009). One of the important questions is whether climate change played a role in this severe drought: was the Millennium Drought consistent with the response of the three dominant climate modes to climate change? This paper aims to provide an overarching review of the recent research that was stimulated by the recent drought, focusing on changes in rainfall.

a. Regional rainfall during the Millennium Drought

Significant rainfall declines have been observed throughout southern and eastern Australia since the mid-to-late twentieth century (CSIRO 2012a). These include a prominent reduction in mid-to-late autumn rainfall over southeast Australia (Fig. 1a; Cai et al. 2012; Murphy and Timbal 2008; Nicholls 2010) and a recent decade-long rainfall deficit in spring (Fig. 1c; Ummenhofer et al. 2009), a summer decline over eastern Queensland since the 1970s (Fig. 1d; Cai et al. 2010), and

Denotes Open Access content.

Corresponding author address: Wenju Cai, CSIRO Marine and Atmospheric Research, PMB 1, Aspendale VIC 3195, Australia.
E-mail: wenju.cai@csiro.au

DOI: 10.1175/JCLI-D-13-00322.1

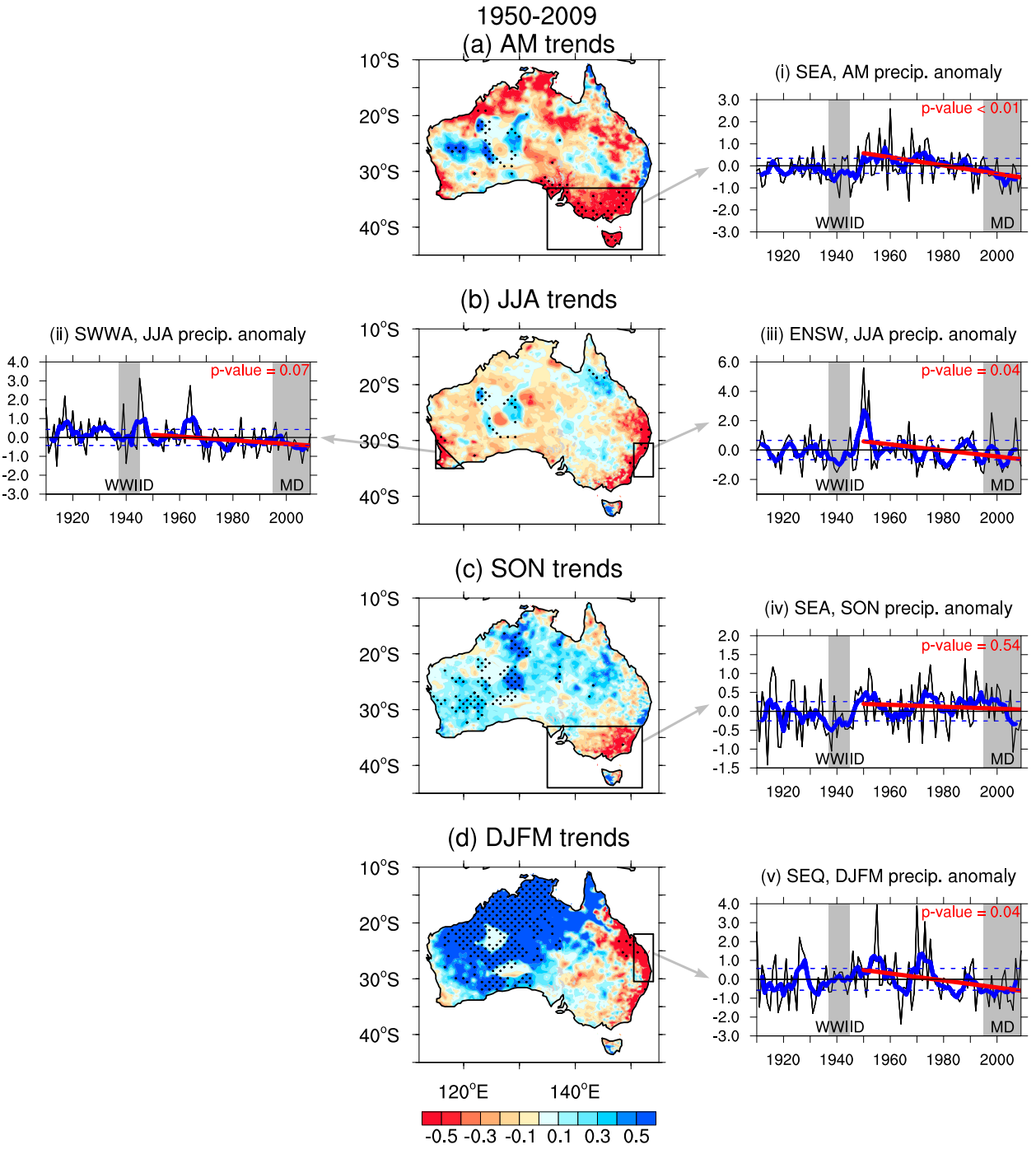

FIG. 1. Observed rainfall trend maps for (a) mid-to-late autumn (AM), (b) winter (JJA), (c) spring (SON), and (d) summer (DJFM) over 1950–2009. Trends are shaded with units of millimeters per day. Stippling indicates regions where the trends are statistically significant at the 95% level as determined by a two-sided *t* test. Boxes indicate the regions over which rainfall is averaged for the time series panels. Time series of rainfall anomalies (referenced to 1900–90 climatology) over 1910–2009 for southeast Australia (SEA) in (a); southwest Western Australia (SWWA) and eastern New South Wales (ENSW) in (b); SEA in (c); and southeast Queensland (SEQ) in (d). Time series are shown in black and the zero line is marked. A 5-yr running average is superimposed on time series in blue, and the dashed blue lines indicate the standard deviation of this running average. Trend lines and *p* values for 1950–2009 are shown in red.

a longer-term decline since the late 1960s in winter over southwest Western Australia (SWWA; Fig. 1b; Cai and Cowan 2006; Hope et al. 2006; Bates et al. 2008). However, it was the severe rainfall deficiencies during the Millennium Drought (approximately 1995–2009) that resulted in critical water shortages across southern and eastern Australia, with unprecedentedly low water levels in many regions leading to strict water restrictions. Facing the possibility of running out of water, many states opted to build water desalination plants to secure long-term water supply, in addition to a substantial short-term investment in water tanks and in research on water recycling, reuse, and storm water harvesting (e.g., CSIRO 2012b).

Over southeast Australia, the largest rainfall decrease is in autumn (April–May) and is statistically significant [Fig. 1a(i); p value < 0.01], with sustained declines during the drought period (Cai et al. 2012). If trends are taken over successive decades (1960 or 1970; not shown), they remain significant, which suggests that the onset of the rainfall reduction commenced long before the Millennium Drought, following on from an anomalously wet multidecade period beginning in the 1950s. The decline during the Millennium Drought is part of the long-term decline. The autumn rainfall reduction is accompanied by local rising mean sea level pressure (MSLP; Larsen and Nicholls 2009; Hope et al. 2010; Nicholls 2010). The exact cause of the autumn decrease, however, remains contentious; the decrease in May accounts for more than 50% of the total autumn trend and may be affected by ENSO variability and a long-term Indian Ocean warming pattern that shifts and weakens southern Australian rain-bearing systems (Cai and Cowan 2008). Late autumn rainfall is also influenced by a weakening of the subtropical storm track due to the decreasing baroclinic instability of the subtropical jet and increasing instability in the polar latitudes (Frederiksen et al. 2011b) and a poleward shift of the ocean–atmosphere circulation (Cai and Cowan 2013a). The well-documented poleward expansion of the subtropical dry zone (Fu et al. 2006; Hu and Fu 2007; Seidel et al. 2008; Johanson and Fu 2009; Lucas et al. 2012), particularly during April–May, is shown to account for much of the autumn rainfall reduction across southeast Australia (Cai et al. 2012).

Throughout SWWA, a 20% reduction in winter rainfall since the late 1960s (e.g., Smith et al. 2000) has led to a significant drop in inflow of more than 50% into the region's water catchments. Following the late 1960s step change in rainfall, a further decline was observed during the Millennium Drought period [Fig. 1b(ii)]. Over 1950–2009 the trend is not significant (p value > 0.05), reflecting the nature of the rainfall decline, which is not purely linear, but rather a step transition from one rainfall regime to another (Hope et al. 2010). In 2010, SWWA experienced its driest winter since records began in 1900 (Bureau of Meteorology 2010a; Cai et al. 2011b). The rainfall decline, along with a reduction in extreme rainfall events (Li et al. 2005), has been linked to multidecadal variability (Cai et al. 2005), changes in large-scale MSLP (Bates et al. 2008), a poleward shift in synoptic systems (Hope et al. 2006), changes in baroclinicity (Frederiksen and Frederiksen 2007; Frederiksen et al. 2011a,b), an upward trend of the SAM and the nonlinearity of its impact (Cai et al. 2011b, and references therein), and Indian Ocean warming trends (Ummenhofer et al. 2008).

Rainfall trends over southeast Australia in spring are weaker than in autumn and highly insignificant from 1950 [Fig. 1c(iv); p value $= 0.54$], as most of the deficit occurs in the mid-1990s (Ummenhofer et al. 2009). The weak spring rainfall decline does, however, display coherence with an intensification in the subtropical ridge (Timbal and Drosdowsky 2013, and references therein). Spring rainfall is also linked to trends and variability in the IOD (Ummenhofer et al. 2009), which has displayed an unprecedentedly high frequency of positive events during recent decades (Ihara et al. 2008; Abram et al. 2008; Cai et al. 2009b). High numbers of positive IOD events tend to be associated with prolonged dry periods across southeast Australia (Ummenhofer et al. 2011); these IOD events not only weaken heavy rainfall over southeast Australia during winter and spring but also increase the risk of hotter spring extreme temperatures (Min et al. 2013). Positive IOD events also increase the risk of major bushfire occurrences across the southern Australian states, as was witnessed in February 2009 (Cai et al. 2009a; Bureau of Meteorology 2010b).

The southeast Queensland summer rainfall decline since the midtwentieth century is statistically significant [Fig. 1d(v)], however, symptomatic of wet decades during the 1950s and 1970s. The wet decade spike in the 1950s is also observed across eastern Australia in winter [Fig. 1b(iii)]. If trends are taken over 1960–2009 instead, they are not statistically significant (not shown). This suggests that the summer drought over southeast Queensland and winter drought across eastern Australia prior to 2009 might not be part of a long-term declining trend [Figs. 1b(iii),d(v)], but associated with the interdecadal Pacific oscillation (IPO), which modulates the influence from ENSO on decadal time scales (Power et al. 1999, 2006; Cai et al. 2010; Speer et al. 2011; Gergis and Ashcroft 2012). During a positive phase of the IPO, such as that which persisted from the late 1970s to 2007 (Cai et al. 2010), the eastern equatorial Pacific is warmer than average (Power et al. 2006), moving the location of the

atmospheric convection center eastward. Even with a La Niña–induced westward shift, the convection center is still too far east to influence northeast Australia: conditions that lead to a prolonged drought. Since 2008, the IPO has switched to its negative phase (Cai and van Rensch 2012), and an influence from consecutive La Niña events combined with anomalously warm local sea surface temperatures (SSTs) contributed to extreme rainfall in 2010 and 2011 (Cai and van Rensch 2012; Evans and Boyer-Souchet 2012).

b. *Climate change and the Millennium Drought: An important issue*

The decade-long duration, unprecedented severity, and vast spatial coverage of the Millennium Drought occurred in a period in which many of the warmest years in terms of global mean temperature were also recorded (CSIRO and Bureau of Meteorology 2012). The extent to which global warming–induced circulation changes have played a part in the drought is a question that has attracted strong public and scientific interest. In terms of the three climate variability modes, there was an unprecedentedly high frequency of positive IOD events (Cai et al. 2009d), a general lack of La Niña events in the 2000s (Ummenhofer et al. 2009), and an upward trend of the SAM (e.g., Marshall 2003; Purich et al. 2013). Thus, the recent behavior of these three modes may have contributed in various degrees to the drought conditions across southern Australia, as in other drought periods (e.g., Verdon-Kidd and Kiem 2009).

An approach to unravel how global warming might have contributed to the drought is through the examination of decadal averages in rainfall (e.g., Gallant et al. 2012). Another is to examine long-term trends and climate mode indices to see whether the severity of the drought may have been a result of natural variability imposed on a long-term climate change–induced decline in rainfall. To this end, it is useful to examine if such decadal averages and trends are generated in a multimodel ensemble average (MMEA) of climate models forced by natural and anthropogenic factors that induce climate change. This approach is useful because variability-induced trends, although present in individual models, are independent from model to model. Thus, a MMEA largely removes natural variability (e.g., Purich et al. 2013), to give a climate change estimate, common across all models. The MMEA approach is also applied to calculate decadal regional rainfall averages and long-term trends that are congruent with trends in the modeled climate indices. This reveals whether the influence on rainfall occurs through a response of the modes of variability to climate change. To achieve this we use the latest generation of global coupled climate models from phase 5 of the the Coupled Model Intercomparison Project (CMIP5; Taylor et al. 2012).

The remainder of this paper is organized as follows: the data and methods used in this study are presented (section 2), then we describe the observed teleconnection of Australian rainfall with the three modes of variability that influence Australia's climate (section 3) before investigating the regional rainfall deficit during the Millennium Drought in the context of decadal averages and long-term trends (section 4). We then evaluate climate model simulations of variability modes and their impact on rainfall (section 5) and the extent to which the rainfall trends are congruent with trends in climate modes (section 6).

2. Data and methods

In this study, we focus on trends in Australian rainfall, and its influence on drought, rather than on other drought indicators such as soil moisture content (e.g., Ummenhofer et al. 2011). To investigate factors responsible for such rainfall trends, we use monthly observations and CMIP5 climate model data, averaged over the four austral seasons defined in this study: autumn [April–May (AM)], winter [June–August (JJA)], spring [September–November (SON)], and summer [December–March (DJFM)]. For Australia, March is a transition month during which the climate is characterized with features that typically resemble a dry summer climate in southern Australia and a monsoon regime in the north, and therefore it is grouped with the summer months. Linear trends in rainfall, and the metrics of ENSO, IOD, SAM[1], and the Southern Hemisphere (SH) subtropical Hadley cell edge (HCE) are calculated over 1950–2009 for the observations and 1950–2005 for the models; 2005 being the last year of their respective historical experiments (Taylor et al. 2012).

In our analysis, ENSO and the SAM are calculated using empirical orthogonal function (EOF) analysis so that variations in the spatial patterns among different models are accounted for (e.g., Saji and Yamagata 2003). The IOD is not defined using EOF analysis—as without detrending prior to analysis (as in Weller and Cai 2013), the IOD and a basinwide IOD-like warming mode are poorly separated (Zheng et al. 2013), leading to an ambiguous IOD signal. The ENSO index is defined as the principal component time series of the first EOF of SST anomalies in the tropical Pacific Ocean, over

[1] The SAM index trend is calculated from 1957, as it is corrected to the Marshall definition (Marshall 2003).

20°S–20°N, 120°E–80°W (similar to Saji and Yamagata 2003). To test the sensitivity to this ENSO definition, an alternative index is calculated [the Niño-3.4 index; areal average SST in the equatorial Pacific Ocean (5°S–5°N, 120°–170°W)], and the results are found to be robust (not shown). The IOD is defined using the dipole mode index (DMI), which is the SST difference across the western and eastern tropical Indian Ocean (Saji et al. 1999); it has been used in various modeling and observational studies (e.g., Cai et al. 2013, and references therein). We restrict our analysis to the DMI definition over winter and spring, when the IOD peaks. The SAM index is defined as the principal component time series of the first EOF of MSLP anomalies from 20° to 90°S (Purich et al. 2013). To test the sensitivity to this SAM definition, an alternate index is calculated (the difference between normalized zonal-mean MSLP at 40° and 65°S, as in Ho et al. 2012), and it is found that varying the SAM definition does not alter the results. The HCE is calculated using the meridional mass streamfunction definition (Johanson and Fu 2009), with the position described as the subtropical latitude where the meridional mass streamfunction at 500 hPa becomes zero (~30°–40°S). This definition has been used extensively in observational and modeling studies (Hu and Fu 2007; Son et al. 2009; Cai et al. 2012; Min and Son 2013; Purich et al. 2013).

Rainfall observations at a resolution of 0.05° × 0.05° are utilized from the Australian Bureau of Meteorology (Jones et al. 2009). To calculate the observational ENSO and IOD indices, SST is taken from the Met Office Hadley Centre Sea Ice and Sea Surface Temperature dataset (HadISST; Rayner et al. 2003) and bilinearly interpolated to a 1° × 1° grid. To calculate the observational SAM index, MSLP is taken from the National Centers for Environmental Prediction–National Center for Atmospheric Research reanalysis (NNR; Kalnay et al. 1996) and also bilinearly interpolated to a 1° × 1° grid. However, it is known that spurious trends exist in the NNR at southern high latitudes (Marshall 2003); to correct for this, MSLP is regressed onto an observational station-based SAM index before EOF analysis (Marshall 2003; Purich et al. 2013). For consistency, the observed HCE is calculated from NNR meridional winds.

We utilize outputs of precipitation (42 models), SST (29 models), MSLP (38 models), and meridional wind (42 models) from the CMIP5 historical experiment archive, as listed in Table 1 (Taylor et al. 2012). All model output is bilinearly interpolated to a 1° × 1° grid. For the modeled trend and regression spatial patterns, one simulation from each model is used (r1i1p1), to avoid weighting models with more than one simulation. For the scatterplots showing individual model trends, all available simulations for each model are used, and for MMEA scatterplots, ensemble averages are used where available, but each model is weighted equally. Multimodel trends in precipitation and climate indices are determined by first calculating the MMEA time series for each variable, and then calculating the trend of this averaged time series. The statistical significance of the trends is based on a two-sided t test, while for the drought anomaly composites, the significance is a t test based on the difference of two means (drought period and climatological period; 1900–90).

Rainfall trends are investigated over the whole of Australia; however, we focus on four defined regions as shown in Fig. 1: southeast Queensland (between 22° and 30.5°S, east of 150.5°E), eastern New South Wales (between 30.5° and 36.5°S, east of 150.5°E), southeast Australia (south of 33°S, east of 135°E), and SWWA (southwest of the line joining 30°S, 115°E and 35°S, 120°E). All four regions experienced widespread rainfall deficiencies during the Millennium Drought (Fig. 1).

For each climate mode (ENSO, IOD, SAM, and HCE), we use climate models forced with climate change over the twentieth century to examine (i) whether there are long-term trends in the indices; (ii) whether there is an associated coherent teleconnection pattern similar to that observed (i.e., Fig. 2); and (iii) whether the rainfall trends are consistent with the response of major modes of climate variability. The climate index–congruent precipitation trend [Rain-trend$|_{\rm ind}(x, y)$] is determined for each model by regressing the linearly detrended rainfall [Rain$|_{\rm dt}(x, y, t)$] at each grid point onto the linearly detrended climate index [Index$|_{\rm dt}(t)$] and multiplying by the climate index trend (Index-trend); that is,

$$\text{Rain-trend}\big|_{\rm ind}(x,y) = \text{regression}[\text{Rain}\big|_{\rm dt}(x,y,t), \text{Index}\big|_{\rm dt}(t)] \times \text{Index-trend}. \quad (1)$$

This is carried out for the observations and for each model and then averaged across all models (e.g., Thompson and Solomon 2002; Cai et al. 2009d; Purich et al. 2013). Statistical significance for the congruent trends is based on a two-sided t test; regions that show significance are where the regression and index trend values are both significant.

3. Impact of climate variability on observed Australia rainfall

In this section, we briefly describe the influence of the climate modes on Australian precipitation over 1950–2009,

TABLE 1. CMIP5 models used in this study. Precipitation and meridional wind data for each model listed are used. Because of the data availability at the time of analysis, SST and MSLP data are not used for some models as noted by the footnotes.

Model	Model expansion	Modeling group
ACCESS1.0	Australian Community Climate and Earth-System Simulator (ACCESS), version 1.0	Commonwealth Scientific and Industrial Research Organisation (CSIRO) and Bureau of Meteorology (BoM), Australia
ACCESS1.3	ACCESS, version 1.3	
BNU-ESM*	Beijing Normal University (BNU)–Earth System Model	College of Global Change and Earth System Science (GCESS), China
CCSM4	Community Climate System Model, version 4	National Center for Atmospheric Research (NCAR), United States
CESM1 (BGC)*	Community Earth System Model (CESM), version 1–Biogeochemistry	National Science Foundation (NSF), U.S. Department of Energy (DOE), and NCAR, United States
CESM1 (CAM5)*	CESM, version 1 (Community Atmosphere Model, version 5)	
CESM1 (CAM5.1–FV2)**	CESM, version 1 (Community Atmosphere Model, version 5.1 and second-order finite volume dynamical core)	
CESM1 (FASTCHEM)*	CESM, version 1 (with FASTCHEM)	
CESM1 (WACCM)*	CESM, version 1 (Whole Atmosphere Community Climate Model)	
CMCC-CM	CMCC Climate Model	Centro Euro-Mediterraneo per i Cambiamenti Climatici (CMCC), Italy
CNRM-CM5	CNRM Coupled Global Climate Model, version 5	Centre National de Recherches Météorologiques (CNRM) and Centre Européen de Recherche et de Formation Avancée en Calcul Scientifique (CERFACS), France
CSIRO Mk3.6.0	CSIRO Mark, version 3.6.0	CSIRO and Queensland Climate Change Centre of Excellence (QCCCE), Australia
CanESM2	Second Generation Canadian Earth System Model	Canadian Centre for Climate Modelling and Analysis (CCCma), Canada
EC-EARTH**	—	EC-Earth Consortium, Europe
FGOALS-g2	Flexible Global Ocean–Atmosphere–Land System Model gridpoint, version 2.0	State Key Laboratory of Numerical Modeling for Atmospheric Sciences and Geophysical Fluid Dynamics (LASG) and Center for Earth System Science (CESS), Tsinghua University, China
FGOALS-s2	Flexible Global Ocean–Atmosphere–Land System Model, second spectral version	LASG and Institute of Atmospheric Physics (IAP), China
FIO-ESM	FIO Earth System Model	First Institute of Oceanography (FIO), China
GFDL-CM2p1**	GFDL Climate Model, version 2.1	National Oceanic and Atmospheric Administration (NOAA) Geophysical Fluid Dynamics Laboratory (GFDL), United States
GFDL-CM3	GFDL Climate Model, version 3	
GFDL-ESM2G	GFDL Earth System Model with Generalized Ocean Layer Dynamics (GOLD) component	
GFDL-ESM2M	GFDL Earth System Model with Modular Ocean Model 4 (MOM4) component	
GISS-E2-H	GISS Model E2, coupled with the Hybrid Coordinate Ocean Model (HYCOM)	National Aeronautics and Space Administration (NASA) Goddard Institute for Space Studies (GISS), United States
GISS-E2-R	GISS Model E2, coupled with the Russell ocean model	
HadGEM2-AO	Hadley Centre Global Environment Model (HadGEM), version 2 - Atmosphere and Ocean	National Institute of Meteorological Research (NIMR) and Korea Meteorological Administration (KMA), Korea
HadCM3	Hadley Centre Coupled Model, version 3	Met Office Hadley Centre (MOHC), United Kingdom
HadGEM2-CC	HadGEM, version 2 - Carbon Cycle	
HadGEM2-ES	HadGEM, version 2 - Earth System	
IPSL-CM5A-LR	IPSL Coupled Model, version 5A, coupled with Nucleus for European Modelling of the Ocean (NEMO), low resolution	L'Institut Pierre-Simon Laplace (IPSL), France
IPSL-CM5A-MR	IPSL Coupled Model, version 5A, coupled with NEMO, mid resolution	
IPSL-CM5B-LR	IPSL Coupled Model, version 5B, low resolution	

TABLE 1. (*Continued*)

Model	Model expansion	Modeling group
MIROC-ESM*	MIROC, Earth System Model	Model for Interdisciplinary Research on Climate (MIROC), Japan
MIROC-ESM-CHEM*	MIROC, Earth System Model, Chemistry Coupled	
MIROC5	MIROC, version 5	
MPI-ESM-LR	MPI Earth System Model, low resolution	Max Planck Institute (MPI), Germany
MPI-ESM-MR	MPI Earth System Model, medium resolution	
MPI-ESM-P*	MPI Earth System Model, paleo	
MRI-CGCM3	MRI Coupled Atmosphere–Ocean General Circulation Model, version 3	Meteorological Research Institute (MRI), Japan
NorESM1-M	Norwegian Earth System Model (NorESM), version 1 (intermediate resolution)	Norwegian Climate Centre (NCC), Norway
NorESM1-ME	NorESM, version 1, intermediate resolution, with prognostic biogeochemical cycling	
BCC_CSM1.1*	BCC, Climate System Model, version 1.1	Beijing Climate Center (BCC), China
BCC_CSM1.1(m)**	BCC, Climate System Model, version 1.1, with moderate resolution	
INM-CM4.0	INM Coupled Model, version 4.0	Institute of Numerical Mathematics (INM), Russia

* SST data not available (ENSO and IOD not calculated).
** SST data not available (ENSO and IOD not calculated) and MSLP data not available (SAM not calculated).

assuming linearity. We note the impact from these modes varies on decadal time scales (e.g., Power et al. 1999), and the correlation pattern may vary depending on the exact period over which the analysis is conducted.

a. Teleconnection with ENSO

ENSO triggers tropical and extratropical teleconnections through its SST and associated convection variations. The tropical teleconnection is an equatorially trapped, deep baroclinic response to the diabatic convective heating anomalies induced by tropical SST anomalies (Gill 1980). The atmospheric manifestation of this direct tropical teleconnection is the Southern Oscillation, of which the impact is mainly confined to near-tropical latitudes and can affect eastern and northeastern Australian rainfall in most seasons except for April–May (Figs. 2a–d). The tropical diabatic heating anomalies also excite equivalent-barotropic Rossby wave trains that propagate into the extratropics (Hoskins and Karoly 1981). However, the anomaly centers are located in the southern South Pacific and have no direct pathway of influence to southern Australia (Fig. 9 of Cai et al. 2011a). Instead, ENSO is able to influence southern Australia's climate through its coherence with the IOD, which operates in winter and spring (IOD and ENSO winter correlation of 0.40, p value < 0.002; spring correlation of 0.60, p value < 0.001), generating Pacific–South America (PSA)-equivalent wave train patterns (section 3b). Often El Niño is associated with a positive IOD (Ummenhofer et al. 2011), during which SSTs off the Sumatra–Java coast are cooler than normal, but warmer than normal over the western tropical Indian Ocean (Saji et al. 1999). Over 1950–2009, this pathway appears to operate not only during spring, but also winter, with associated rainfall anomalies seen along the inland eastern region of Australia, but not along the eastern seaboard (Fig. 2b), indicating an eastward-propagating signal. However, since the late 1970s, variations in ENSO have been only weakly coherent with variations in the IOD during winter; therefore, the Indian Ocean teleconnection pathway for ENSO has predominantly occurred in spring (Cai et al. 2011a).

As the IOD does not operate during summer, ENSO's influence is largely conducted via the near-tropical response, but is also modulated by an Indian Ocean basin mode (Chambers et al. 1999; Klein et al. 1999; Xie et al. 2009), which is in part induced by and highly coherent with ENSO. The basinwide warming mode generates an equivalent-barotropic Rossby wave train through convection anomalies over northern Australia. The wave train shares an anomaly center over Tasman Sea latitudes with the PSA pattern, shifting the anomaly center of the PSA pattern closer to Australia, and thus affecting southeast Australia (Cai and van Rensch 2013).

b. Impact from the IOD

Tropical and extratropical responses are also associated with the IOD during winter and spring (Saji and Yamagata 2003; Cai et al. 2011a). The equivalent-barotropic Rossby waves emanating from the east pole (winter) and from both poles (spring) of the IOD, referred to respectively as the eastern and western Indian Ocean wave trains, are major pathways whereby the IOD impact is conveyed to mid- to high-latitude regions (Cai et al. 2011a). A result of the wave trains is the presence of an anticyclone south of Australia during

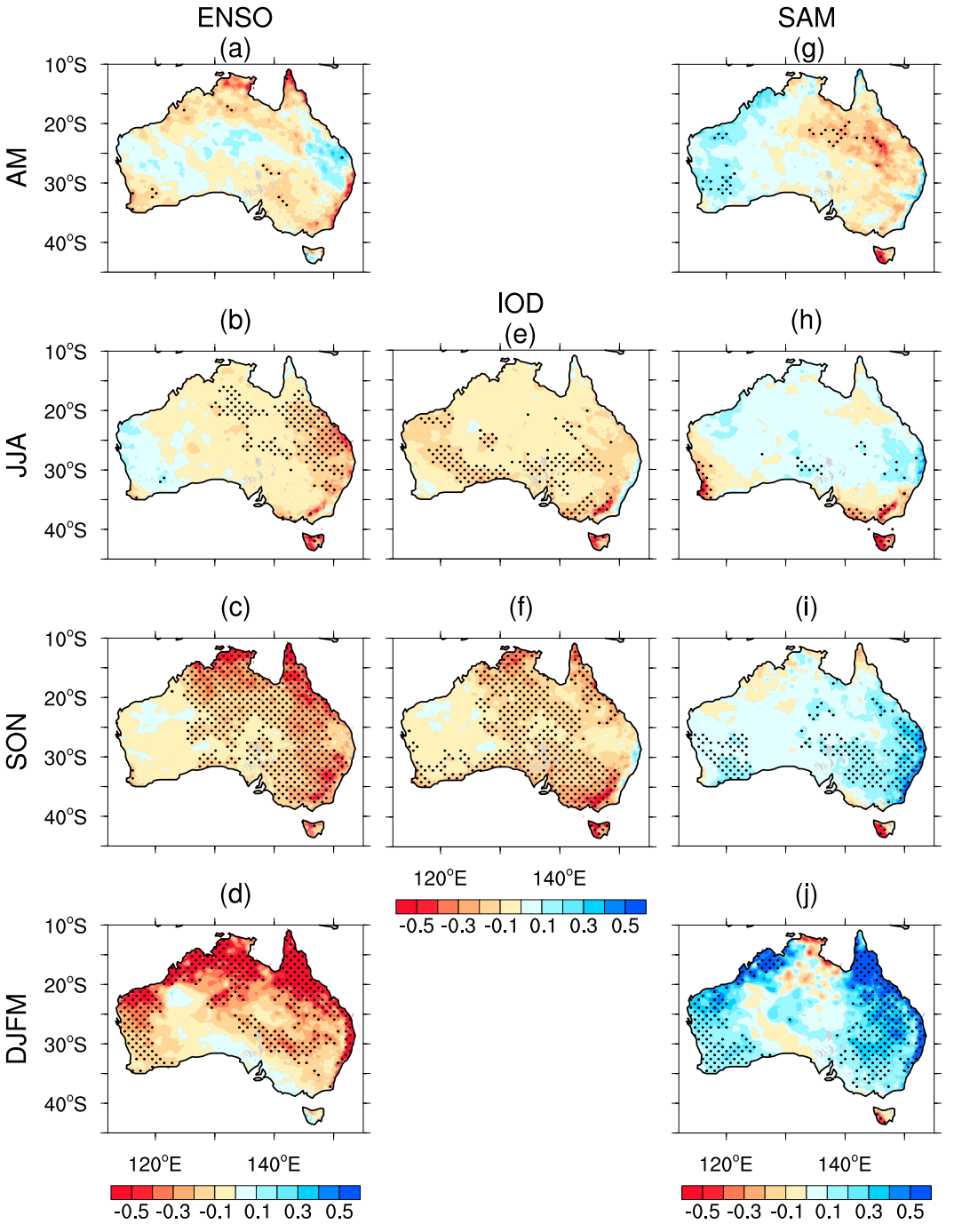

FIG. 2. Regression maps of gridded observed Australian rainfall onto observed climate indices using detrended data from 1950 to 2009 for AM, JJA, SON, and DJFM: (a)–(d) ENSO, (e)–(f) IOD (only JJA and SON), and (g)–(j) SAM (over 1957–2009). ENSO and SAM indices are defined by EOF and the IOD is defined using the DMI. Regression coefficients are multiplied by one standard deviation of the relevant climate index to give units of millimeters per day. Stippling indicates regions where the regression coefficients are statistically significant at the 95% level as determined by a two-sided *t* test.

a positive IOD, influencing southern Australian winter rainfall (Fig. 2e). During spring this high pressure center is located slightly eastward, and the corresponding area of influence covers most of central and southeast Australia (Fig. 2f). The anticyclone induces a poleward shift in the positions of rain-bearing weather systems that pass by southern Australia, thus reducing rainfall frequency and intensity.

c. *Influence of the SAM*

The SAM exhibits a strong seasonal impact predominantly associated with the seasonal movement of the extratropical westerly jet. In April–May, the mean latitude of the jet is not close enough to Australian latitudes for anomalous poleward movements associated with the SAM to affect rainfall variability over southern Australia (Fig. 2g). During winter the mean jet is located closer to the equator, shifting westerly weather systems northward such that they affect southern Australia. A positive phase of the SAM is associated with a poleward contraction in the mean jet and the westerly weather systems, leading to anomalously dry winter conditions across southeast and southwest Australia (Fig. 2h; e.g., Cai and Cowan 2006; Hendon et al. 2007; Hope et al. 2010). In spring and summer, the mean jet is sufficiently poleward such that westerly winds do not prevail, allowing easterly weather systems to bring moist onshore flow to eastern Australia. A positive SAM and the associated poleward shift of the westerly jet promote development of such easterly weather systems, occasionally through blocking high events, leading to increased rainfall over eastern Australia (Hendon et al. 2007; Cowan et al. 2013; Pook et al. 2013).

d. *Impact from Hadley cell edge variability*

Another process that influences rainfall variability is the poleward movement of the SH HCE, which describes a zonal average of the large-scale atmospheric vertical circulation that carries rising tropical heat and moisture poleward to the extratropics (e.g., Hu and Fu 2007). The regions beneath the descending branches of the Hadley cell are marked as subtropical dry zones (Seidel et al. 2008). Variability of the HCE and a poleward expansion of the dry zone have been used to explain the observed mid-to-late autumn rainfall reduction over southeast Australia (Cai et al. 2012). Prior to the 1980s, an anomalous poleward expansion of the subtropical dry zone was associated with anomalously low rainfall over southern Australia (Figs. 3a–c of Cai et al. 2012). However since the 1980s, this relationship has been absent, as the HCE has moved beyond southern Australia latitudes such that variations no longer have a signature in rainfall (Figs. 3d–f of Cai et al. 2012).

4. Historical context of the Millennium Drought rainfall deficit

a. *Comparison with the World War II Drought (1936–45)*

One way to place the Millennium Drought in historical context is to compare it with the World War II (WWII) Drought: the preceding severe drought to affect much of Australia (Verdon-Kidd and Kiem 2009; Ummenhofer et al. 2009). Rainfall averages over two 10-yr periods (1936–45 and 2000–09) reveal commonalities and differences (Fig. 3). First, a mid-to-late autumn rainfall deficit is seen in both periods: during the WWII Drought the deficit was wide spread (Fig. 3a), but during the Millennium Drought it is concentrated and more severe over eastern and southeast Australia (Fig. 3e). Second, during both droughts, winter rainfall deficit over southeast Australia displays a similar pattern (Figs. 3b,f), except over Tasmania. This may be due to regional orographic influences across Tasmania's west coast or the dominance of particular climate modes during the different decades, such as PSA suppression of positive SAM and El Niño events (Hill et al. 2009). However, during the WWII drought winter rainfall over SWWA is actually above the 1900–90 average, in sharp contrast to the Millennium Drought, when a significantly low rainfall anomaly is observed (Fig. 3f). Third, both droughts feature lower rainfall anomalies over southeast Australia during spring (Figs. 3c,g), although the deficit during the Millennium Drought is less severe (Verdon-Kidd and Kiem 2009) and mainly confined to eastern coastal Victoria than that during the WWII Drought. The similarity in the winter and spring patterns between the two droughts suggests common dynamics; both periods feature a high frequency of positive IOD events (Cai et al. 2009c,d; Ummenhofer et al. 2009). Finally, although both droughts feature only a small summer rainfall reduction over southeast Australia, the rainfall deficit over eastern Australia is substantial (Figs. 3d,h). Sparsely populated northwest Australia experienced dry conditions during the WWII Drought, but a strong increase in rainfall during the Millennium Drought; however, this is not the focus of this study.

Based on comparison of the rainfall anomaly composites during these two drought periods, only the Millennium Drought autumn deficit in southeast Australia and the winter deficit in SWWA are more severe than regional/seasonal deficits during the WWII Drought. This suggests that, with the exception of the southeast Australia autumn and SWWA winter deficits, the severe conditions observed during the Millennium Drought can be induced by natural variability alone, as they have been observed previously during a period with little climate change forcing.

b. *Observed rainfall trends congruent with trends in climate indices*

Given the impact of the three main climate modes on rainfall, we examine whether trends in their indices contribute to the long-term rainfall trends over 1950–2009.

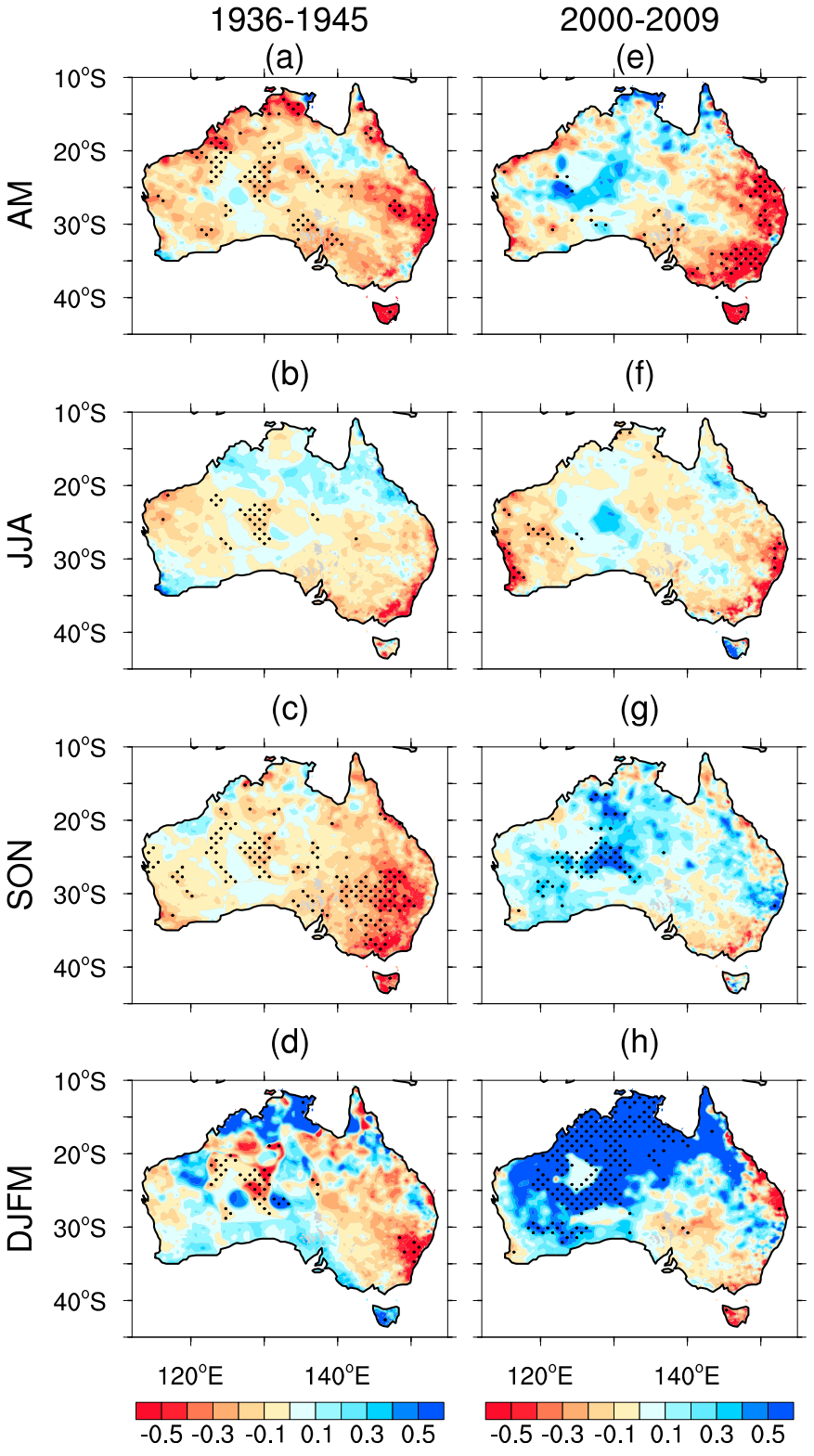

FIG. 3. The 10-yr-averaged observed rainfall anomalies (referenced to 1900–90 climatology) for AM, JJA, SON, and DJFM: (a)–(d) World War II Drought (1935–46) and (e)–(h) Millennium Drought (2000–09). Anomalies are shaded with units of millimeters per day. Stippling indicates regions where the anomalies are significantly different from the climatology at the 95% level as determined by a two sided *t* test.

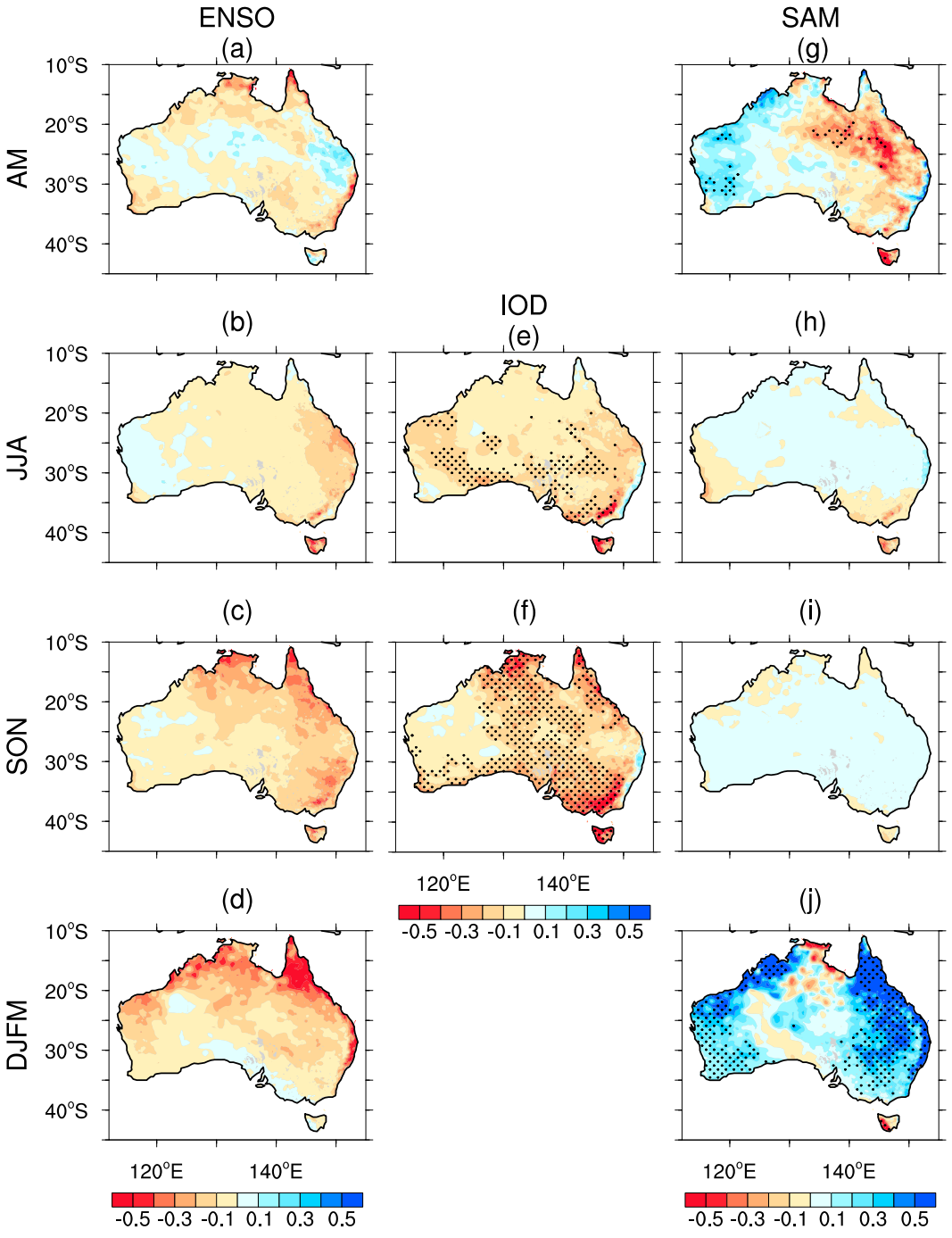

FIG. 4. As in Fig. 2, but the regression coefficients have been multiplied by observed trends in relevant climate indices to give climate index–congruent trends in gridded Australian rainfall. Trends are over 1950–2009 for AM, JJA, SON, and DJFM: (a)–(d) ENSO, (e)–(f) IOD (only JJA and SON), and (g)–(j) SAM (over 1957–2009). Trends are shaded with units of millimeters per day.

We use Eq. (1) to analyze the observed congruent trends (Fig. 4). This reveals that despite the broad ENSO impact across most seasons (Figs. 2a–d), a lack of statistically significant trends in the observed ENSO index means there is little ENSO-congruent trend in any season (Figs. 4a–d). Trends congruent with the IOD contribute to a scattered winter and a broad spring rainfall reduction over southern Australia (Figs. 4e–f), consistent with an upward trend of the IOD during these seasons (Ihara et al. 2008; Abram et al. 2008; Cai

et al. 2009c,d). Although an upward trend of the winter SAM should contribute to a winter rainfall reduction over SWWA and parts of southeast Australia (Fig. 4h), trends in the SAM are not statistically significant during winter over this period; however, DJFM SAM trends are significant, and as such would contribute to a summer rainfall increase over much of eastern Australia (Hendon et al. 2007). Thus, the weak ENSO trend generates a weak summer rainfall decrease, largely offset by the SAM-induced rainfall increase. These long-term offsetting trends are opposite to their impacts on interannual time scales, in which El Niño is associated with negative SAM (Codron 2005; L'Heureux and Thompson 2006; Fogt and Bromwich 2006; Pohl et al. 2010), both leading to reduced summer rainfall across eastern Australia.

We have not explicitly addressed the impact from a poleward shift of the HCE. As this is a position index, it makes little sense to apply a detrending procedure, as the application would potentially impose a nonmeaningful relationship to regions where fluctuations of the HCE no longer show coherence with rainfall. Therefore, the procedure of seeking congruent trends cannot be used. This is shown to be the case in the post-1980 period for April–May (Cai et al. 2012); the descending branch of the SH HCE has passed beyond Australian latitudes such that its fluctuation no longer influences southeast Australian rainfall. Despite this, there is a strong correlation between the SAM and HCE indices (Purich et al. 2013). Therefore, the impact of the HCE may be gauged through the impacts of the SAM.

5. Model simulation of climate variability impact on Australia rainfall

Before assessing the climate variability impact on Australian rainfall as simulated by CMIP5 models, it is first important to assess how well these models simulate the variability of the climate modes and regional rainfall on interannual and interdecadal time scales. The modeled spatial patterns of the first EOF of SST in the tropical Pacific Ocean reasonably represent an ENSO-like pattern when compared to observations (not shown). The first EOF pattern in the observations accounts for approximately 48%, 55%, 68%, and 65% of their total variance in AM, JJA, SON, and DJFM, respectively. In the models, the first EOF accounts for 28%–69%, 37%–70%, 47%–77%, and 37%–78% of the variance in AM, JJA, SON, and DJFM, respectively.

The observed and modeled IOD are described by the DMI because of the ambiguity assigning the correct EOF pattern to the IOD when the SST data are not detrended prior to analysis. For example, Zheng et al. (2013) showed that the IOD spatial pattern variances range from 7% to 34% for 17 CMIP5 models over the period 1900–2005, with some models unable to simulate the eastern pole of the IOD in the Sumatra–Java region. For both JJA and SON, the models tend to simulate DMI variability higher than that observed (Cai and Cowan 2013b), although the spread of modeled standard deviations encompasses the observed. For JJA, the range of standard deviations in the modeled DMI is 0.25–0.77 (average of 0.44), while the observed standard deviation is 0.33. For SON, the range of standard deviations in the modeled DMI is 0.34–1.24 (average of 0.74), while the observed standard deviation is 0.36.

The spatial pattern of the first EOF of MSLP in the extratropical SH is found to reasonably represent a SAM-like pattern when compared to the observations (not shown). The uncorrected NNR SAM pattern (i.e., the spatial pattern of the first EOF of NNR MSLP that has not been regressed onto the Marshall SAM index) accounts for approximately 34%, 37%, 28%, and 42% of the variance in AM, JJA, SON, and DJFM, respectively. In the models, the first EOF accounts for 22%–54%, 27%–61%, 32%–63%, and 23%–75% of the variance in AM, JJA, SON, and DJFM, respectively. These results are similar to other EOF representations of the SAM in CMIP5 models (e.g., Purich et al. 2013).

An assessment of the models' ability to simulate regionally and seasonally averaged precipitation decadal variability is undertaken (not shown). For the regions and seasons of interest here, the observed decadal variability is within the spread of variability displayed by individual models, except for eastern New South Wales in JJA, where all models substantially underestimate decadal variability. For both southeast Australia and SWWA in JJA, although the observations lie within the intermodel spread, the majority of models underestimate the decadal standard deviations of rainfall.

Based on outputs from the CMIP5 climate models, the teleconnections of Australian rainfall with ENSO, the IOD, and the SAM are constructed using a MMEA. While an overall pattern resembling that observed is generated for the IOD and SAM from winter through to summer, and for ENSO in spring and summer, unrealistic features also exist. For ENSO, there is a weak (and insignificant) modeled teleconnection in April–May, similar to what is observed (Figs. 2a, 5a). In winter, the observations show a broad teleconnection over eastern Australia; however, the models underestimate the impact, in part atributable to the averaging across models (Fig. 5b), although the modeled maximum is located in the central east coast as for observations. In spring, a broader spatial teleconnection pattern is generated by the models, with a somewhat realistic

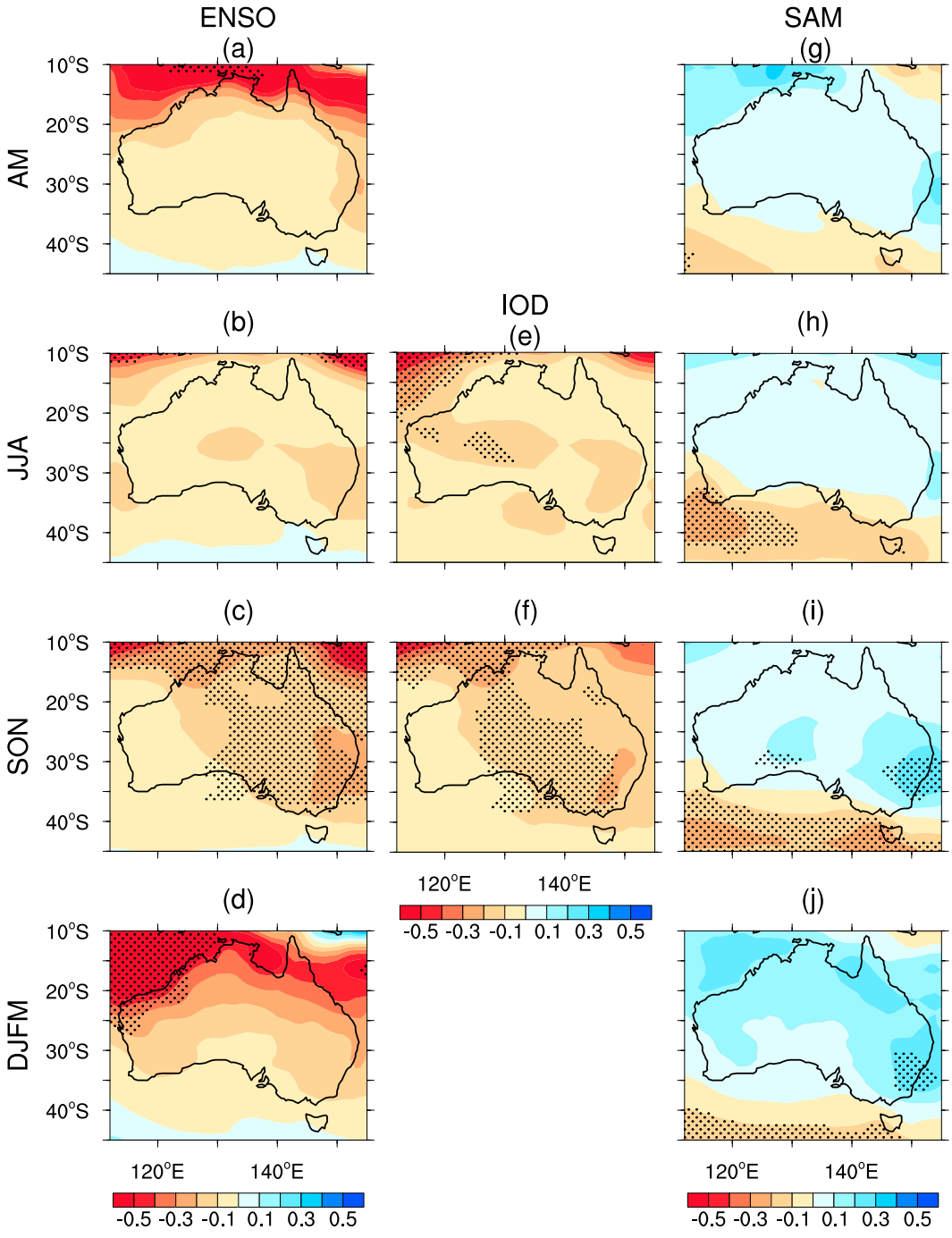

FIG. 5. As in Fig. 2, but for the CMIP5 MMEA over 1950–2005. The first run (r1i1p1) of each available model is included in the ensemble: 29 models are used in (a)–(d) ENSO and (e)–(f) IOD, and 38 models are used in (g)–(j) SAM. The regression coefficients for each model are first calculated and multiplied by one standard deviation of the relevant climate index to give units of millimeters per day, and the MMEA determined by averaging across models. Stippling indicates regions where the average regression coefficient is statistically significant at the 95% level as determined by a two-sided *t* test.

distribution across the eastern half of Australia, although this is again generally weaker in magnitude than that observed (Fig. 5c). The modeled extension of the ENSO impact into southeast Australia is conducted through coherence with the model IOD, similar to that observed (Cai et al. 2011a; Weller and Cai 2013). Because of the model resolution, the teleconnection pattern displayed by the MMEA in spring lacks detailed

orographic features, which would have confined the ENSO impact inland of the east Australian coast (as in Fig. 2d). During the summer months (Fig. 5d), the simulated teleconnection patterns are quite unrealistic; instead of a teleconnection over northeast Australia, the maximum correlation is situated over northwest Australia. This discrepancy is similar to that seen in the CMIP phase 3 (CMIP3) models (Cai et al. 2010).

For the IOD, the pattern of teleconnection in winter lacks significance across southeastern Australia compared to the observations; however, it is comparable during spring, particularly over southeast Australia (Figs. 5e,f). The observed impact of the IOD on southern Australia is conducted through Rossby wave trains emanating from the eastern Indian Ocean that affect the frequency, intensity, and position of the weather systems (Cai et al. 2011a). The majority of climate models reasonably simulate this pathway (Weller and Cai 2013). The large impact seen in spring across the central northwest region reflects the more developed and coherent relationship between the IOD and ENSO.

The impact of the SAM is simulated reasonably well by the MMEA. A rainfall-increasing effect in summer and spring over much of Australia (Figs. 5i,j) and a rainfall-decreasing influence over southwest Australia during winter (Fig. 5h) are captured by the MMEA. However, the impact on southeast Australia during winter is weaker than that observed and is not statistically significant. In April–May, the SAM has no statistically significant impact over Australia (Fig. 5g), similar to what has been found for the full autumn season (Cai and Cowan 2013a).

6. Simulated Australian rainfall trends congruent with trends in modes of variability

A MMEA of the regional rainfall time series allows the extent to which rainfall changes are attributable to climate change to be gauged. A rainfall anomaly in any given historical model experiment contains a component that is forced by climate change and a component that is attributable to internal natural variability. A separation of these components is somewhat possible through the MMEA process, as the independent internal variability of each simulation is cancelled out in a MMEA, leaving predominantly the common climate change component (Hegerl et al. 2007). This multimodel, finger-printing process has been used extensively in previous studies to distinguish the roles of anthropogenic and natural forcings on climate trends (e.g., Gleckler et al. 2012). A MMEA of rainfall trends (Figs. 6a–d) and comparison with those observed (Fig. 1), however, suggests that the rainfall decline over most regions since 1950 may not be attributable to climate change, with the exception of the winter rainfall reduction over SWWA.

The differences between the observed and modeled trends since 1950 are analyzed further in Fig. 6e for selected regions that observed a long-term rainfall decline (regardless of significance). The MMEA does not implicate climate change in the observed April–May rainfall reduction over southeast Australia, with only about half of the models producing a reduction in the April–May rainfall and none producing a reduction even half the magnitude of that observed (Fig. 7a). The models' inability might be due to a deficiency in producing the associated dynamics of the poleward expansion of the subtropical dry zone (Lu et al. 2007), as discussed below. By contrast, the majority of models are able to simulate a winter rainfall reduction in SWWA comparable to that observed (Fig. 7b); thus, over SWWA, about half of the observed winter rainfall decline since 1950 is attributable to climate change (Fig. 6e), consistent with results using CMIP3 output (Cai and Cowan 2006). Despite the large observed declines in southeast Queensland summer rainfall, the MMEA actually indicates a weak rainfall increase, as a result of the modeled SAM rainfall coherence in this region (Fig. 5j).

Comparing rainfall anomalies during the Millennium Drought period to the WWII Drought period is useful to determine whether similar anomalies occurred during a period with little climate change forcing, and thus whether natural variability alone may account for such anomalies. Figure 8 shows the regionally averaged observed (blue) and MMEA (red) decade-long rainfall anomalies for the WWII (Fig. 8a) and Millennium (Fig. 8b) Droughts. During the WWII Drought, all of the MMEA anomalies are close to zero, as would be expected as climate change forcing during this period was minimal, and thus the effects of climate change were minor. The observed rainfall deficit in southeast Australia during spring is statistically significant, but all other rainfall anomalies are insignificant. This indicates that for southeast Australia, strong decadal rainfall deficits during spring may result from natural variability alone. In Fig. 8b, it can be seen that the observed rainfall anomalies in southeast Australia during autumn and SWWA during winter are statistically significant. However, only the SWWA winter rainfall deficit can be partially attributed to climate change, as this is the only region/season where the MMEA also exhibits a statistically significant anomaly. Based on this, it is likely that climate change did contribute to part of the Millennium Drought in SWWA. It is uncertain whether the strong autumn rainfall deficit in southeast Australia is attributable to natural variability alone, as climate models

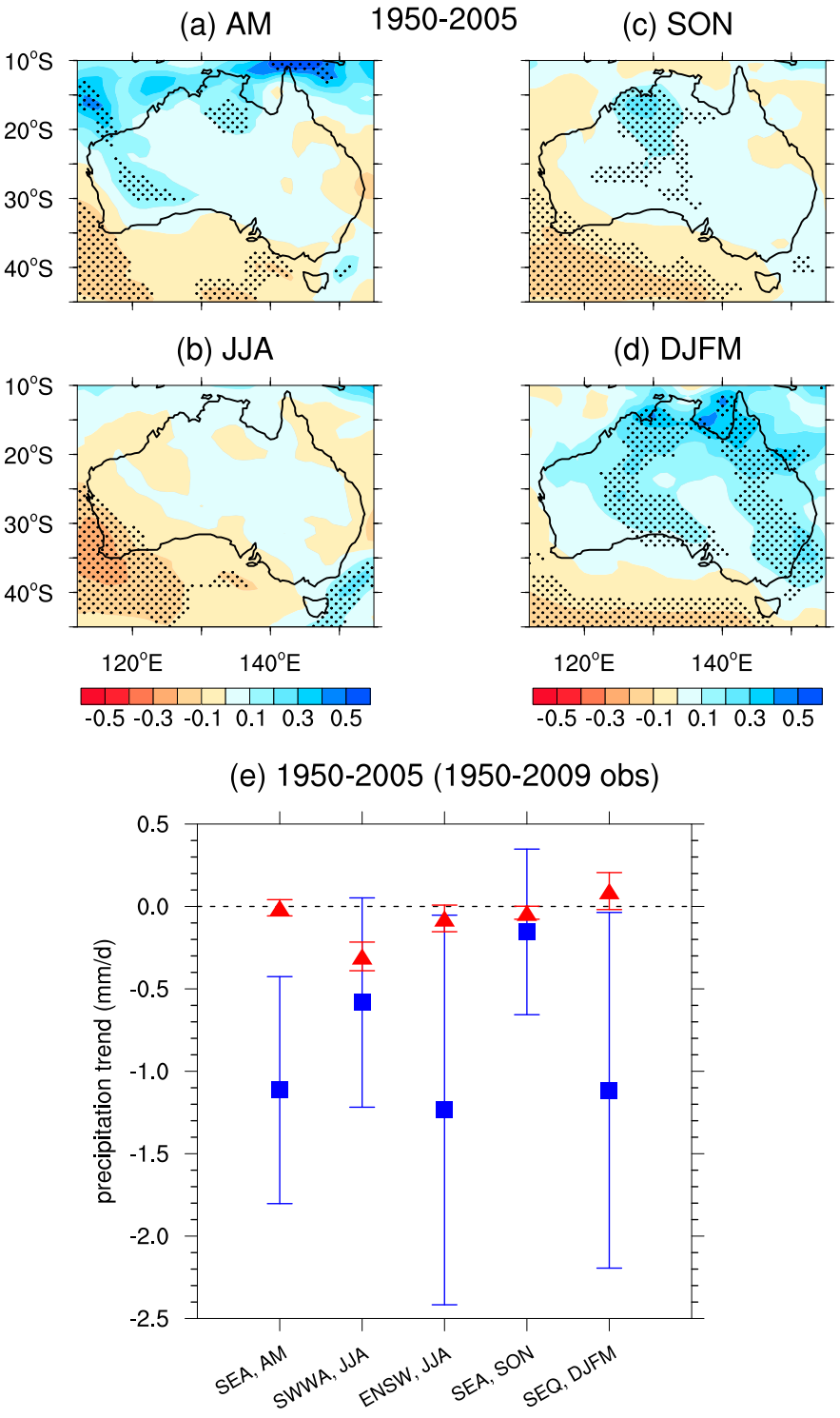

FIG. 6. (a)–(d) As in Figs. 1a–d, but for the CMIP5 MMEA over 1950–2005. The first run (r1i1p1) of each available model is included in the ensemble: 42 models are used. A multimodel-averaged precipitation time series is first calculated, and the trend determined from this series. Trends are shaded with units of millimeters per day. Stippling indicates regions where the average trend is statistically significant at the 95% level as determined by a two-sided t test. (e) Summary of regional rainfall total trends for the MMEA (red triangles; 1950–2005) and observations (blue squares; 1950–2009) for AM over SEA; JJA over SWWA and ENSW; SON over SEA; and DJFM over SEQ. Ensemble averages for individual models are used in the MMEA. Error bars show the 2.5% and 97.5% confidence levels associated with trends.

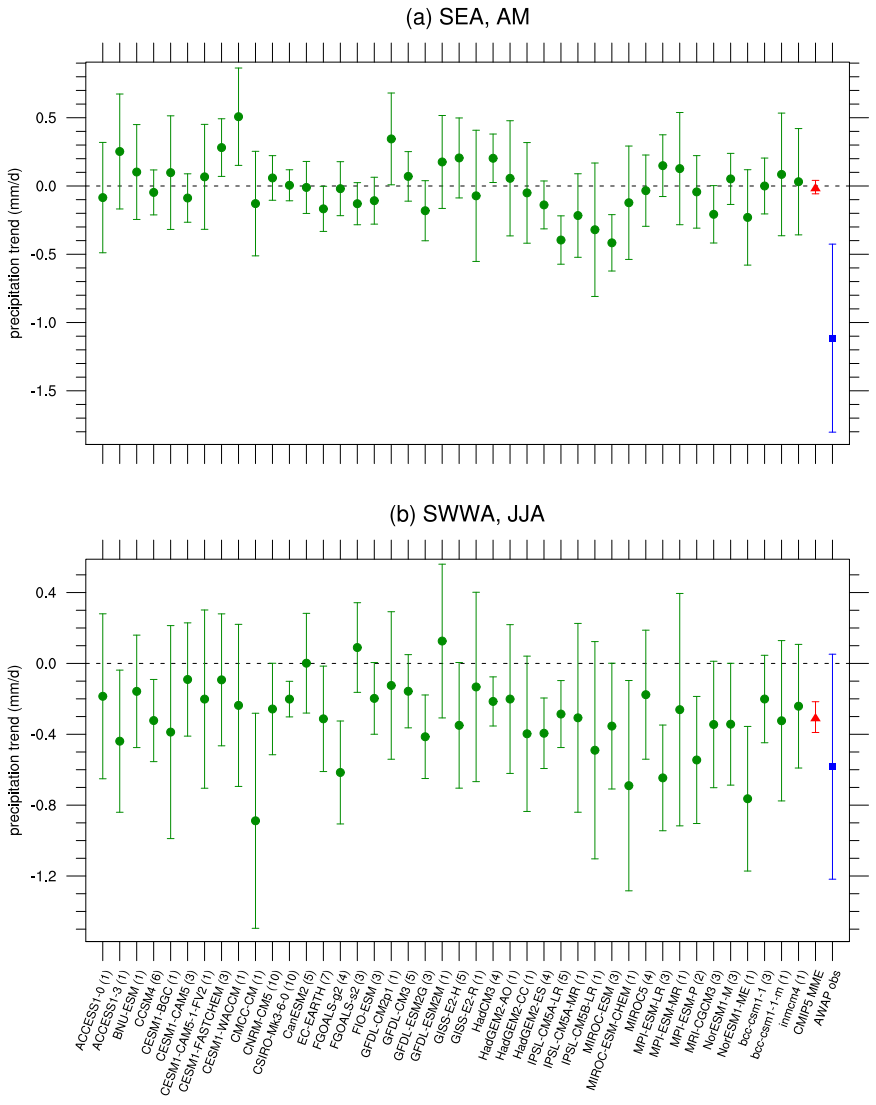

FIG. 7. Examples of individual model (green circles; 1950–2005), MMEA (red triangles; 1950–2005), and observed (blue squares; 1950–2009) spread in total rainfall trends: (a) AM over SEA, and (b) JJA over SWWA. Where multiple runs for individual models are available, an ensemble average is first calculated. The number of runs for each model is indicated in brackets next to the model name. Error bars show the 2.5% and 97.5% confidence levels associated with trends.

underestimate some of the processes that may have been responsible for the rainfall deficit, such as the poleward shift of the HCE.

We next examine simulated rainfall trends congruent with trends in modes of variability. The individual and cumulative effects of congruent trends must both be considered, as there is a possibility that the contribution of individual modes is correct in sign, but that their relative importance is different in the models compared to the observations.

Figure 9 shows the simulated seasonal trends in ENSO, the IOD, the SAM, and the HCE, while Figs. 10 and 11 display the associated rainfall trend patterns. There is a statistically significant positive trend in the modeled ENSO index in each season, comparable in magnitude to that observed (Fig. 9a). These trends result in a rainfall reduction in all seasons, generally consistent with that observed (Fig. 4), but because the modeled ENSO teleconnection pattern is weak, the congruent trend is also weak and generally insignificant, except during spring over eastern and central Australia (Figs. 10a–d). It is interesting that the ENSO-congruent trend produces a rainfall reduction over northwest Australia (Fig. 10d): an artifact of the unrealistic ENSO teleconnections in the

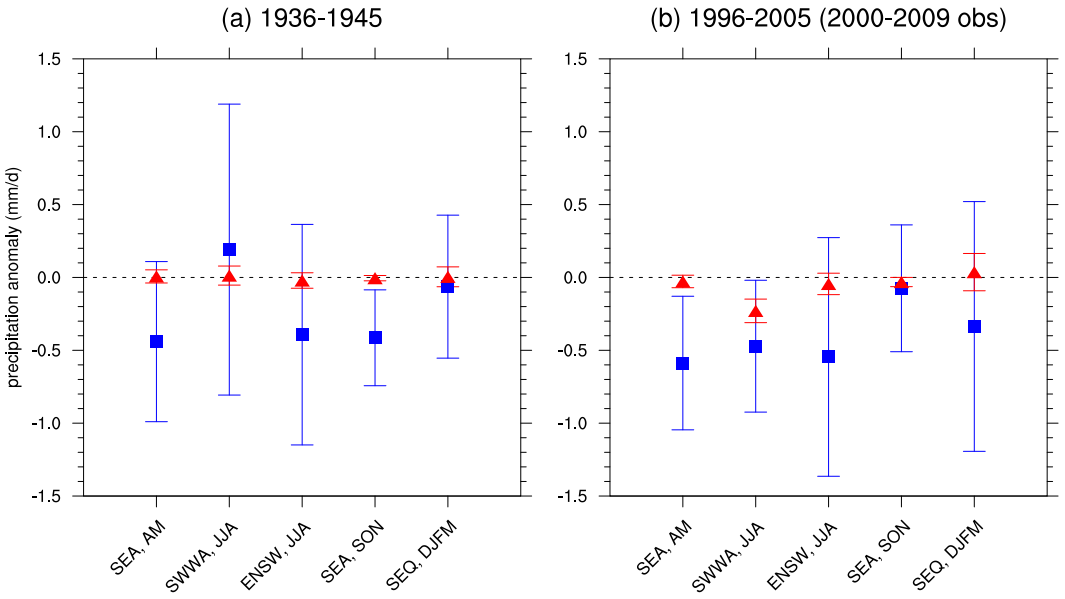

FIG. 8. Summary of 10-yr-averaged rainfall anomalies (referenced to 1900–90 climatology) for the MMEA (red triangles) and observations (blue squares) for AM over SEA; JJA over SWWA and ENSW; SON over SEA; and DJFM over SEQ. (a) World War II Drought (1935–46) and (b) Millennium Drought (MMEA 1996–2005; observations 2000–09). Where multiple runs for individual models are available, an ensemble average is first calculated, and this ensemble averaged used in the MMEA. Error bars show the 2.5% and 97.5% confidence levels.

climate models, linked to a western Pacific SST bias (Weller and Cai 2013).

In both winter and spring, the modeled IOD trends are considerably weaker than observed; however, both modeled trends are statistically significant and are within the observed confidence limits (Fig. 9b). The IOD trend in the CMIP3 models over 1950–99 has been shown to be about 80% of a standard deviation (Cai et al. 2009c); however, the reason for the weak IOD trends in CMIP5 models remains poorly understood. Nevertheless, they translate to weaker IOD-congruent rainfall trends in the models compared to the observed, although the sign of the MMEA congruent change in spring is consistent with the observed (cf. Figs. 4e,f and 10e,f). Note that although modeled trends are weakly significant in Fig. 9b, in Figs. 10e,f no significance is seen as a slightly different subset of the models is used (individual model ensemble averages are used in Fig. 9b where available, but not in Figs. 10e,f). In the MMEA, the IOD-congruent trend is not consistent with the modeled total rainfall trend (Fig. 6c), suggesting that an offsetting trend congruent with other modes is also important.

The MMEA SAM trend is largest in summer (Fig. 9c), but the corrected reanalyses show the largest trend in April–May, followed by summer. This discrepancy is consistent with previous studies on the simulation of SAM trends by models (e.g., Fogt et al. 2009). In winter, the modeled SAM-congruent rainfall trends show a maximum rainfall reduction over SWWA (Fig. 10h), whereas for spring, the SAM-congruent trend leads to an increase in rainfall over eastern Australian (Fig. 10i), offsetting the reduction congruent with ENSO and the IOD. This offsetting effect from a SAM-congruent rainfall increase upon an ENSO-congruent decrease is also seen in summer (Fig. 10j), but the MMEA impact from the SAM appears to dominate that from ENSO, leading to a rainfall increase in eastern New South Wales (Fig. 6d).

The simulated poleward shifts in the SH HCE are far smaller than in reanalysis for all seasons (Fig. 9d). In addition, the majority of the models underestimate decadal variability in the HCE, although the observations lie within the intermodel spread (not shown). As with trends in the SAM, while the simulated maximum shift occurs in summer, the maximum observed shift occurs in April–May. The differences between the magnitudes of the observed and MMEA shifts are considerable; during summer (autumn) the observed trends exceed the MMEA trend by a factor of 4 (6). In the reanalysis, the HCE has shifted beyond the latitudes of southern Australia, such that interannual variability of the HCE no longer influences southern Australia rainfall (Cai et al. 2012). This means that using the sensitivity of observed rainfall to HCE movements and the total shift in the HCE to estimate a trend-congruent rainfall change is not

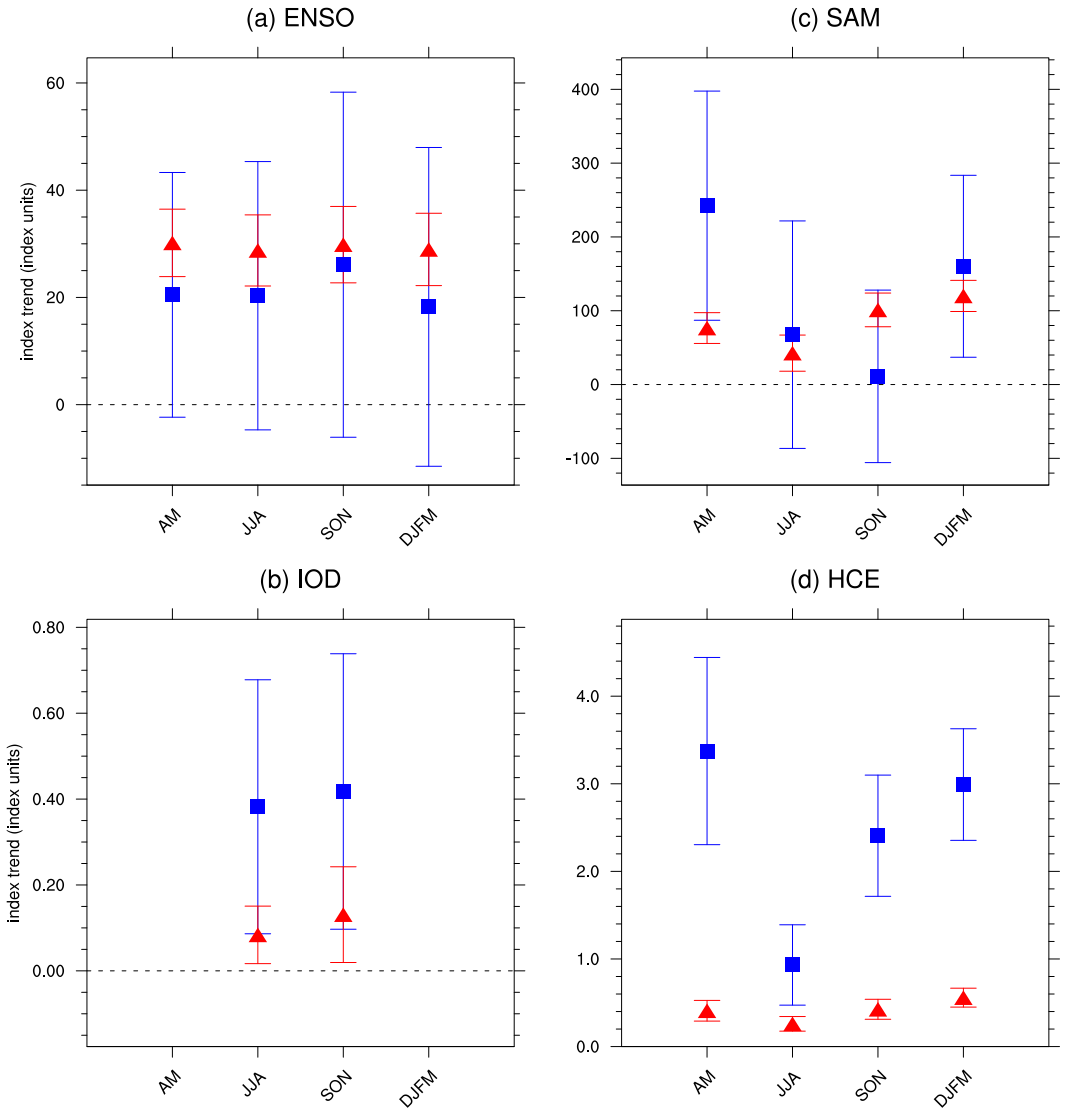

FIG. 9. Summary of seasonal MMEA (red triangles; 1950–2005) and observed (blue squares; 1950–2009) total trends in (a) ENSO (EOF time series units), (b) IOD (°C; JJA and SON only), (c) SAM (EOF time series units), and (d) SH HCE (°lat poleward shift). Where multiple runs for individual models are available, an ensemble average is first calculated, and this ensemble averaged used in the MMEA. Error bars show the 2.5% and 97.5% confidence levels associated with trends.

applicable (Cai et al. 2012). However, because the modeled shift is many times smaller than that observed, in the models the HCE influence has not shifted beyond Australian latitudes, so the HCE-congruent trends in rainfall are calculated (Fig. 11).

A major feature in the MMEA HCE-congruent trends is a rainfall increase across much of Australia in spring and summer, associated with the poleward shift in the HCE and tropical wet-zone expansion (Figs. 11c,d,g,h). In April–May, this wetting process does not influence southeast Australia and SWWA because climatological rainfall to the north of these regions is less than in the regions themselves, such that a poleward HCE shift equates to a dry-zone expansion (rather than a wet-zone expansion; Cai et al. 2012). During winter a poleward expansion of the HCE leads to a slight rainfall reduction in southern coastal regions (Figs. 11b,f). Thus, despite the vast underestimation of the poleward shift of the HCE, the MMEA does suggest that a statistically significant shift occurs because of climate change, and such a shift potentially contributes to autumn and winter rainfall reductions over southern Australia (although such reductions themselves are not statistically significant).

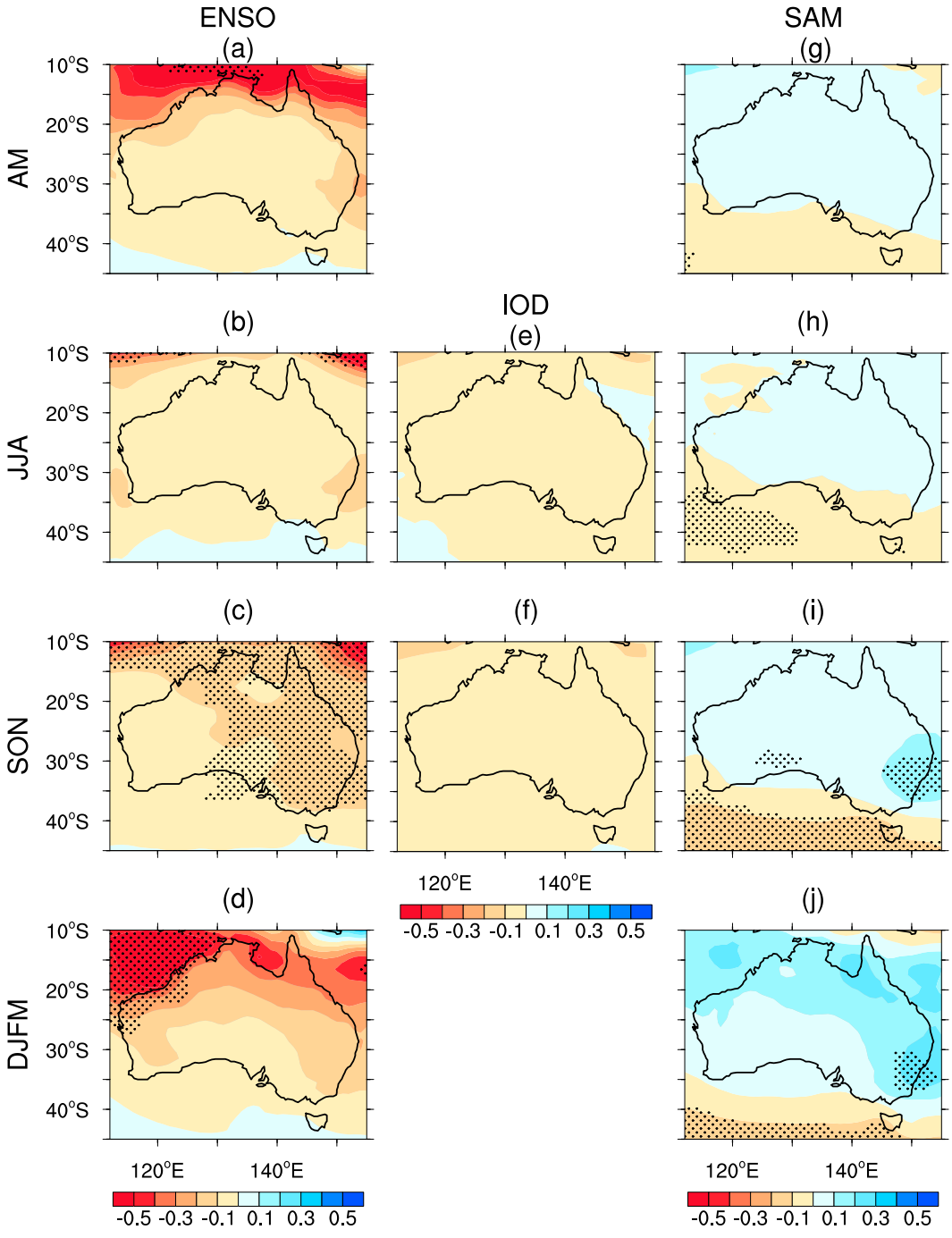

FIG. 10. CMIP5 MMEA seasonal rainfall trends over 1950–2005 congruent with trends in (a)–(d) ENSO, (e)–(f) IOD (only JJA and SON), and (g)–(j) SAM. Congruent trends are determined by calculating the regression coefficient between detrended rainfall and climate indices and multiplying by the trends in the climate indices. Congruent trends are calculated for each model individually and then averaged across models. Trends are shaded with units of millimeters per day. Stippling indicates regions where the average regression coefficient is statistically significant and the relevant climate index trend is also significant, both at the 95% level as determined by a two-sided *t* test.

Throughout this analysis, we have not addressed the interaction between climate modes among these models. It is well known that on seasonal time scales, a positive IOD is often associated with El Niño, which is in turn associated with a negative SAM phase, while a positive SAM often reflects the poleward shift of the HCE (e.g., Risbey et al. 2009). These relationships do not necessarily hold in response to climate change: for example,

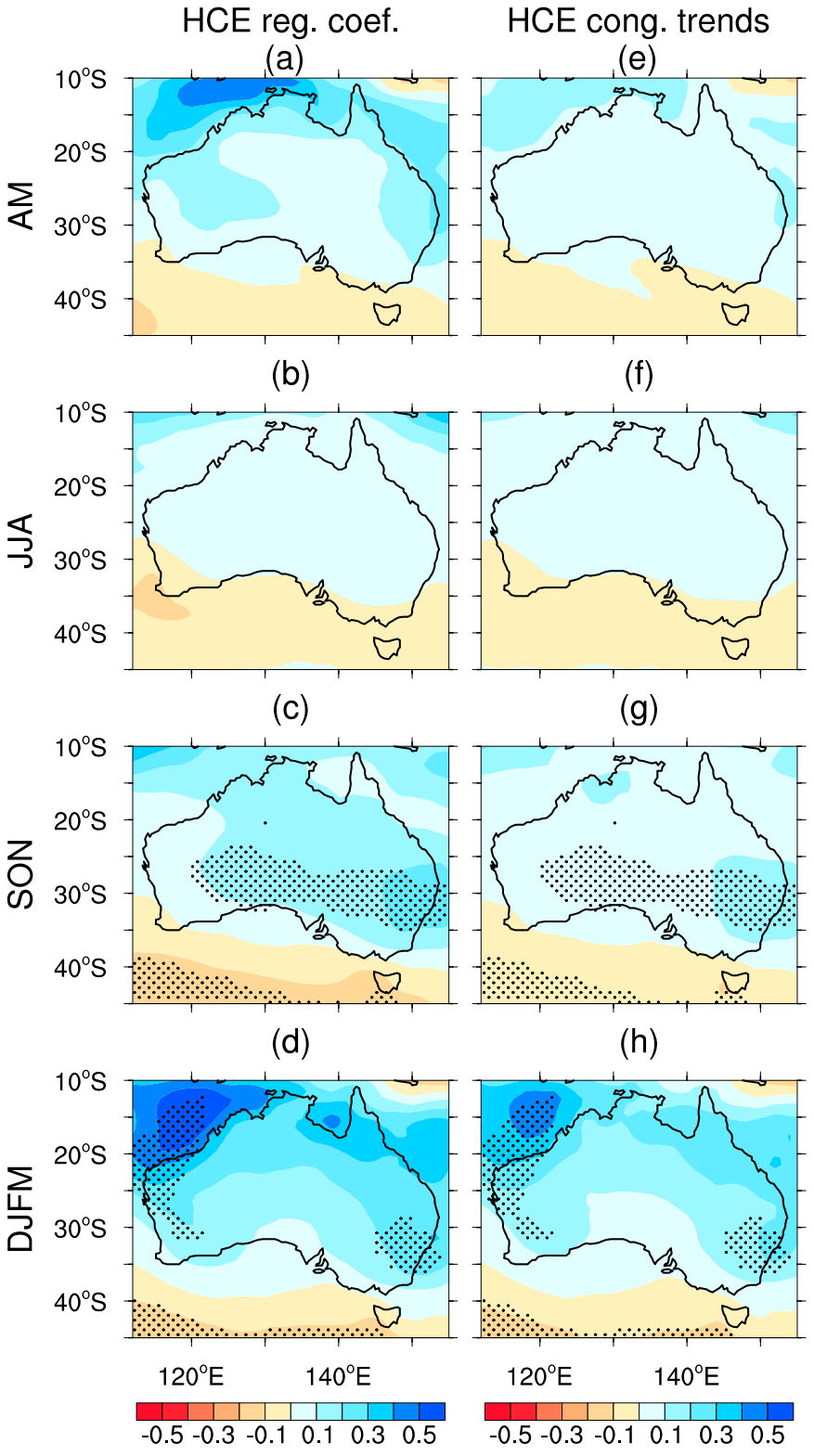

FIG. 11. (a)–(d) As in Fig. 5 and (e)–(h) as in Fig. 10, but for CMIP5 MMEA rainfall regression coefficients and trends congruent with the SH HCE trends. The first run (r1i1p1) of each available model is included in the ensemble: 42 models are used. Stippling indicates statistical significance as in Figs. 5 and 10.

the poleward expansion of the HCE and the positive SAM trend follow their interannual relationship; however, ENSO and the SAM are both trending upward, as opposed to their coherence on interannual time scales (Wang and Cai 2013).

7. Conclusions

Spanning from the mid-1990s to the late 2000s, the Millennium Drought was the most severe drought experienced by southern Australia since instrumental record began in the 1900s. Despite its devastating impacts, the drought stimulated a large body of research, which gave rise to a better understanding of the processes associated with Australian rainfall variability on regional scales and the relative importance of climate modes in forcing associated long-term changes. This body of research is greatly aided by the unprecedented data resource of global climate models spanning across two model generations (i.e., CMIP3 and CMIP5) that are used to address whether climate change plays a role in inducing long-term rainfall trends. This study uses CMIP5 model output and examines (i) whether the observed rainfall trend is generated when much of the internal variability is removed through multimodel averaging, and (ii) whether the regional rainfall trends are consistent with the responses of the IOD, ENSO, SAM, and HCE. Decadal-mean anomalies in rainfall during the Millennium Drought are compared to those of the WWII Drought to gain further insight into whether such anomalies have occurred previously because of natural variability alone or were influenced by climate change.

CMIP5 model results confirm that the drought over southern Australia is at least in part attributable to a recent anthropogenic-induced change in the climate: (i) in SWWA an upward SAM trend (although not significant) contributed to the winter rainfall reductions; and (ii) in both SWWA and southeast Australia a poleward shift of the HCE may have partially contributed to the mid-to-late autumn and winter rainfall reductions, despite models severely underestimating the magnitude of this shift. The changes in these climate indices are partially attributable to greenhouse warming, despite the weak climate change fingerprint in the Millennium Drought in the models across eastern and southeast regions. This conclusion considers only rainfall changes during the drought and does not consider the unprecedented high temperatures experienced during the Millennium Drought compared to the WWII Drought (e.g., Ummenhofer et al. 2009). It is not clear how our results may be affected by model deficiencies associated with model resolution (e.g., Grose et al. 2012) and tropical biases such as the equatorial Pacific cold tongue, the double intertropical convergence zone (Hwang and Frierson 2013), and the overly strong variability of the IOD (Cai and Cowan 2013b), which have implications for SH circulation and rainfall patterns.

Trends in the SAM and the HCE have also mitigated drought in other regions. In spring and summer, both the SAM and HCE trends are shown to induce a congruent rainfall-increasing trend in coastal regions of eastern Australia (e.g., Kang et al. 2011), compensating rainfall-reducing drivers and leading to little change in annual rainfall trends. The summer rainfall decline in southeast Queensland is not attributable to climate change, but strongly linked to multidecadal variability (e.g., Cai et al. 2010), and in this region CMIP5 models show an offsetting tendency between the impact of the SAM and ENSO trends.

The natural progression of this study is to examine whether observed rainfall changes are consistent with what is expected in the future under the projected CMIP5 scenarios, and this awaits investigation.

Acknowledgments. This study is supported by the Goyder Research Institute and the Australian Climate Change Science Programme. We thank three anonymous reviewers for the helpful comments, which improved this manuscript. We acknowledge the World Climate Research Programme's Working Group on Coupled Modelling, which is responsible for CMIP, and thank the climate modelling groups listed in Table 1 for producing and making available their model output.

REFERENCES

Abram, N. J., M. K. Gagan, J. E. Cole, W. S. Hantoro, and M. Mudelsee, 2008: Recent intensification of tropical climate variability in the Indian Ocean. *Nat. Geosci.,* **1,** 849–853, doi:10.1038/ngeo357.

Ashok, K., Z. Guan, and T. Yamagata, 2003: Influence of the Indian Ocean dipole on the Australian winter rainfall. *Geophys. Res. Lett.,* **30,** 1821, doi:10.1029/2003GL017926.

Bates, B., P. Hope, B. Ryan, I. Smith, and S. Charles, 2008: Key findings from the Indian Ocean climate initiative and their impact on policy development in Australia. *Climatic Change,* **89,** 339–354, doi:10.1007/s10584-007-9390-9.

Bureau of Meteorology, 2010a: A very dry year so far in southwest Western Australia. Bureau of Meteorology, Special Climate Statement 21, 8 pp. [Available online at http://www.bom.gov.au/climate/current/statements/scs21a.pdf.]

——, cited 2010b: Annual Australian climate statement 2009. [Available online at http://www.bom.gov.au/announcements/media_releases/climate/change/20100105.shtml.]

Cai, W., and T. Cowan, 2006: SAM and regional rainfall in IPCC AR4 models: Can anthropogenic forcing account for southwest Western Australian winter rainfall reduction? *Geophys. Res. Lett.,* **33,** L24708, doi:10.1029/2006GL028037.

——, and ——, 2008: Dynamics of late autumn rainfall reduction over southeastern Australia. *Geophys. Res. Lett.,* **35,** L09708, doi:10.1029/2008GL033390.

——, and P. van Rensch, 2012: The 2011 southeast Queensland extreme summer rainfall: A confirmation of a negative Pacific decadal oscillation phase? *Geophys. Res. Lett.,* **39,** L08702, doi:10.1029/2011GL050820.

——, and T. Cowan, 2013a: Southeast Australia autumn rainfall reduction: A climate-change-induced poleward shift of ocean–atmosphere circulation. *J. Climate,* **26,** 189–205, doi:10.1175/JCLI-D-12-00035.1.

——, and ——, 2013b: Why is the amplitude of the Indian Ocean dipole overly large in CMIP3 and CMIP5 climate models? *Geophys. Res. Lett.,* **40,** 1200–1205, doi:10.1002/grl.50208.

——, and P. van Rensch, 2013: Austral summer teleconnections of Indo-Pacific variability: Their nonlinearity and impacts on Australian climate. *J. Climate,* **26,** 2796–2810, doi:10.1175/JCLI-D-12-00458.1.

——, G. Shi, and Y. Li, 2005: Multidecadal fluctuations of winter rainfall over southwest Western Australia simulated in the CSIRO mark 3 coupled model. *Geophys. Res. Lett.,* **32,** L12701, doi:10.1029/2005GL022712.

——, T. Cowan, and M. Raupach, 2009a: Positive Indian Ocean dipole events precondition southeast Australia bushfires. *Geophys. Res. Lett.,* **36,** L19710, doi:10.1029/2009GL039902.

——, ——, and A. Sullivan, 2009b: Recent unprecedented skewness towards positive Indian Ocean dipole occurrences and its impacts on Australian rainfall. *Geophys. Res. Lett.,* **36,** L11705, doi:10.1029/2009GL037604.

——, A. Sullivan, and T. Cowan, 2009c: Climate change contributes to more frequent consecutive positive Indian Ocean dipole events. *Geophys. Res. Lett.,* **36,** L19783, doi:10.1029/2008GL036443.

——, ——, and ——, 2009d: How rare are the 2006–2008 positive Indian Ocean dipole events? An IPCC AR4 climate model perspective. *Geophys. Res. Lett.,* **36,** L08702, doi:10.1029/2009GL037982.

——, P. van Rensch, T. Cowan, and A. Sullivan, 2010: Asymmetry in ENSO teleconnection with regional rainfall, its multidecadal variability, and impact. *J. Climate,* **23,** 4944–4955, doi:10.1175/2010JCLI3501.1.

——, ——, ——, and H. H. Hendon, 2011a: Teleconnection pathways of ENSO and the IOD and the mechanisms for impacts on Australian rainfall. *J. Climate,* **24,** 3910–3923, doi:10.1175/2011JCLI4129.1.

——, ——, S. Borlace, and T. Cowan, 2011b: Does the southern annular mode contribute to the persistence of the multidecade-long drought over southwest Western Australia? *Geophys. Res. Lett.,* **38,** L14712, doi:10.1029/2011GL047943.

——, T. Cowan, and M. Thatcher, 2012: Rainfall reductions over Southern Hemisphere semi-arid regions: The role of subtropical dry zone expansion. *Sci. Rep.,* **2,** 702, doi:10.1038/srep00702.

——, X.-T. Zheng, E. Weller, M. Collins, T. Cowan, M. Lengaigne, W. Yu, and T. Yamagata, 2013: Projected response of the Indian Ocean dipole to greenhouse warming. *Nat. Geosci.,* **6,** 999–1007, doi:10.1038/ngeo2009.

Chambers, D. P., B. D. Tarpley, and R. H. Stewart, 1999: Anomalous warming in the Indian Ocean coincident with El Niño. *J. Geophys. Res.,* **104** (C2), 3035–3047, doi:10.1029/1998JC900085.

Codron, F., 2005: Relation between annular modes and the mean state: Southern Hemisphere summer. *J. Climate,* **18,** 320–330, doi:10.1175/JCLI-3255.1.

Cowan, T., P. van Rensch, A. Purich, and W. Cai, 2013: The association of tropical and extratropical climate modes to atmospheric blocking across southeastern Australia. *J. Climate,* **26,** 7555–7569, doi:10.1175/JCLI-D-12-00781.1.

CSIRO, 2012a: Climate and water availability in south-eastern Australia: A synthesis of findings from phase 2 of the South Eastern Australian Climate Initiative (SEACI). CSIRO Tech. Rep., 41 pp. [Available online at https://publications.csiro.au/rpr/download?pid=csiro:EP127070&dsid=DS3.]

——, 2012b: 5 years of urban water research in South East Queensland 2007-2012. Urban Water Security Research Alliance Tech. Rep., 32 pp. [Available online at http://www.urbanwateralliance.org.au/publications/UWSRA-final-synthesis-report.pdf.]

——, and Bureau of Meteorology, 2012: State of the climate 2012. Commonwealth of Australia, 12 pp.

Evans, J. P., and I. Boyer-Souchet, 2012: Local sea surface temperatures add to extreme precipitation in northeast Australia during La Niña. *Geophys. Res. Lett.,* **39,** L10803, doi:10.1029/2012GL052014.

Fogt, R. L., and D. H. Bromwich, 2006: Decadal variability of the ENSO teleconnection to the high-latitude South Pacific governed by coupling with the southern annular mode. *J. Climate,* **19,** 979–997, doi:10.1175/JCLI3671.1.

——, J. Perlwitz, A. J. Monaghan, D. H. Bromwich, J. M. Jones, and G. J. Marshall, 2009: Historical SAM variability. Part II: Twentieth-century variability and trends from reconstructions, observations, and the IPCC AR4 models. *J. Climate,* **22,** 5346–5365, doi:10.1175/2009JCLI2786.1.

Frederiksen, C. S., J. S. Frederiksen, J. M. Sisson, and S. L. Osbrough, 2011a: Australian winter circulation and rainfall changes and projections. *Int. J. Climate Change: Strategies Manage.,* **3,** 170–188, doi:10.1108/17568691111129002.

——, ——, ——, and ——, 2011b: Changes and projections in the annual cycle of the Southern Hemisphere circulation, storm tracks and Australian rainfall. *Int. J. Climate Change: Impacts Responses,* **2** (3), 143–162.

Frederiksen, J. S., and C. S. Frederiksen, 2007: Interdecadal changes in Southern Hemisphere winter storm track modes. *Tellus,* **59,** 599–617, doi:10.1111/j.1600-0870.2007.00264.x.

Fu, Q., C. M. Johanson, J. M. Wallace, and T. Reichler, 2006: Enhanced mid-latitude tropospheric warming in satellite measurements. *Science,* **312,** 1179, doi:10.1126/science.1125566.

Gallant, A. J. E., K. J. Hennessy, and J. Risbey, 2007: Trends in rainfall indices for six Australian regions: 1910–2005. *Aust. Meteor. Mag.,* **56,** 223–241.

——, M. Reeder, J. Risbey, and K. Hennessy, 2012: The characteristics of seasonal-scale droughts in Australia, 1911–2009. *Int. J. Climatol.,* **33,** 1658–1672, doi:10.1002/joc.3540.

Gergis, J., and L. Ashcroft, 2012: Rainfall variations in south-eastern Australia part 2: A comparison of documentary, early instrumental and palaeoclimate records, 1788–2008. *Int. J. Climatol.,* **33,** 2973–2987, doi:10.1002/joc.3639.

Gill, A. E., 1980: Some simple solutions for heat-induced tropical circulation. *Quart. J. Roy. Meteor. Soc.,* **106,** 447–462, doi:10.1002/qj.49710644905.

Gleckler, P. J., and Coauthors, 2012: Human-induced global ocean warming on multidecadal timescales. *Nat. Climate Change,* **2,** 524–529, doi:10.1038/nclimate1553.

Grose, M., M. Pook, P. McIntosh, J. Risbey, and N. Bindoff, 2012: The simulation of cutoff lows in a regional climate model: Reliability and future trends. *Climate Dyn.,* **39,** 445–459, doi:10.1007/s00382-012-1368-2.

Hegerl, G. C., and Coauthors, 2007: Understanding and attributing climate change. *Climate Change 2007: The Physical Science Basis,* S. Solomon et al., Eds., Cambridge University Press, 663–745.

Hendon, H. H., D. W. J. Thompson, and M. C. Wheeler, 2007: Australian rainfall and surface temperature variations associated with the Southern Hemisphere annular mode. *J. Climate,* **20,** 2452–2467, doi:10.1175/JCLI4134.1.

Hill, K. J., A. Santoso, and M. H. England, 2009: Interannual Tasmanian rainfall variability associated with large-scale climate modes. *J. Climate,* **22,** 4383–4397, doi:10.1175/2009JCLI2769.1.

Ho, M., A. S. Kiem, and D. C. Verdon-Kidd, 2012: The southern annular mode: A comparison of indices. *Hydrol. Earth Syst. Sci.,* **16,** 967–982, doi:10.5194/hess-16-967-2012.

Hope, P., W. Drosdowsky, and N. Nicholls, 2006: Shifts in the synoptic systems affecting southwest Western Australia. *Climate Dyn.,* **26,** 751–764, doi:10.1007/s00382-006-0115-y.

——, B. Timbal, and R. Fawcett, 2010: Associations between rainfall variability in the southwest and southeast of Australia and their evolution through time. *Int. J. Climatol.,* **30,** 1360–1371, doi:10.1002/joc.1964.

Hoskins, B. J., and D. J. Karoly, 1981: The steady linear response of a spherical atmosphere to thermal and orographic forcing. *J. Atmos. Sci.,* **38,** 1179–1196, doi:10.1175/1520-0469(1981)038<1179:TSLROA>2.0.CO;2.

Hu, Y., and Q. Fu, 2007: Observed poleward expansion of the Hadley circulation since 1979. *Atmos. Chem. Phys.,* **7,** 5229–5236, doi:10.5194/acp-7-5229-2007.

Hwang, Y.-T., and D. M. M. Frierson, 2013: Link between the double-intertropical convergence zone problem and cloud biases over the Southern Ocean. *Proc. Natl. Acad. Sci. USA,* **110,** 4935–4940, doi:10.1073/pnas.1213302110.

Ihara, C., Y. Kushnir, and M. A. Cane, 2008: Warming trend of the Indian Ocean SST and Indian Ocean dipole from 1880 to 2004. *J. Climate,* **21,** 2035–2046, doi:10.1175/2007JCLI1945.1.

Johanson, C. M., and Q. Fu, 2009: Hadley cell widening: Model simulations versus observations. *J. Climate,* **22,** 2713–2725, doi:10.1175/2008JCLI2620.1.

Jones, D. A., W. Wang, and R. Fawcett, 2009: High-quality spatial climate data-sets for Australia. *Aust. Meteor. Oceanogr. J.,* **58,** 233–248.

Kalnay, E., and Coauthors, 1996: The NCEP/NCAR 40-Year Reanalysis Project. *Bull. Amer. Meteor. Soc.,* **77,** 437–471, doi:10.1175/1520-0477(1996)077<0437:TNYRP>2.0.CO;2.

Kang, S. M., L. M. Polvani, J. C. Fyfe, and M. Sigmond, 2011: Impact of polar ozone depletion on subtropical precipitation. *Science,* **332,** 951–954, doi:10.1126/science.1202131.

Klein, S. A., B. J. Soden, and N.-C. Lau, 1999: Remote sea surface variations during ENSO: Evidence for a tropical atmospheric bridge. *J. Climate,* **12,** 917–932, doi:10.1175/1520-0442(1999)012<0917:RSSTVD>2.0.CO;2.

Larsen, S. H., and N. Nicholls, 2009: Southern Australian rainfall and the subtropical ridge: Variations, interrelationships, and trends. *Geophys. Res. Lett.,* **36,** L08708, doi:10.1029/2009GL037786.

L'Heureux, M. L., and D. W. J. Thompson, 2006: Observed relationships between the El Niño–Southern Oscillation and the extratropical zonal-mean circulation. *J. Climate,* **19,** 276–287, doi:10.1175/JCLI3617.1.

Li, Y., W. J. Cai, and E. P. Campbell, 2005: Statistical modelling of extreme rainfall in southwest Western Australia. *J. Climate,* **18,** 852–863, doi:10.1175/JCLI-3296.1.

Lu, J., G. A. Vecchi, and T. Reichler, 2007: Expansion of the Hadley cell under global warming. *Geophys. Res. Lett.,* **34,** L06805, doi:10.1029/2006GL028443.

Lucas, C., H. Nguyen, and B. Timbal, 2012: An observational analysis of Southern Hemisphere tropical expansion. *J. Geophys. Res.,* **117,** D17112, doi:10.1029/2011JD017033.

Marshall, G. J., 2003: Trends in the southern annular mode from observations and reanalyses. *J. Climate,* **16,** 4134–4143, doi:10.1175/1520-0442(2003)016<4134:TITSAM>2.0.CO;2.

Min, S.-K., and S.-W. Son, 2013: Multimodel attribution of the Southern Hemisphere Hadley cell widening: Major role of ozone depletion. *J. Geophys. Res.,* **118,** 3007–3015, doi:10.1002/jgrd.50232.

——, W. Cai, and P. Whetton, 2013: Influence of climate variability on seasonal extremes over Australia. *J. Geophys. Res.,* **118,** 643–654, doi:10.1002/jgrd.50164.

Murphy, B. F., and B. Timbal, 2008: A review of recent climate variability and climate change in southeastern Australia. *Int. J. Climatol.,* **28,** 859–879, doi:10.1002/joc.1627.

Nicholls, N., 2010: Local and remote causes of the southern Australian autumn-winter rainfall decline, 1958–2007. *Climate Dyn.,* **34,** 835–845, doi:10.1007/s00382-009-0527-6.

——, B. Lavery, C. Frederiksen, W. Drosdowsky, and S. Torok, 1996: Recent apparent changes in relationships between the El Niño southern oscillation and Australian rainfall and temperature. *Geophys. Res. Lett.,* **23,** 3357–3360, doi:10.1029/96GL03166.

Pohl, B., N. Fauchereau, C. J. C. Reason, and M. Rouault, 2010: Relationships between the Antarctic Oscillation, the Madden–Julian oscillation, and ENSO, and consequences for rainfall analysis. *J. Climate,* **23,** 238–254, doi:10.1175/2009JCLI2443.1.

Pook, M., J. Risbey, P. McIntosh, C. Ummenhofer, A. Marshall, and G. Meyers, 2013: The seasonal cycle of blocking and associated physical mechanisms in the Australian region and relationship with rainfall. *Mon. Wea. Rev.,* **141,** 4534–4553, doi:10.1175/MWR-D-13-00040.1.

Power, S., T. Casey, C. Folland, A. Colman, and V. Mehta, 1999: Interdecadal modulation of the impact of ENSO on Australia. *Climate Dyn.,* **15,** 319–324, doi:10.1007/s003820050284.

——, M. Haylock, R. Colman, and X. Wang, 2006: The predictability of interdecadal changes in ENSO activity and ENSO teleconnections. *J. Climate,* **19,** 4755–4771, doi:10.1175/JCLI3868.1.

Purich, A., T. Cowan, S.-K. Min, and W. Cai, 2013: Autumn precipitation trends over Southern Hemisphere midlatitudes as simulated by CMIP5 models. *J. Climate,* **26,** 8341–8356, doi:10.1175/JCLI-D-13-00007.1.

Rayner, N. A., D. E. Parker, E. B. Horton, C. K. Folland, L. V. Alexander, D. P. Rowell, E. C. Kent, and A. Kaplan, 2003: Global analyses of sea surface temperature, sea ice, and night marine air temperature since the late nineteenth century. *J. Geophys. Res.,* **108,** 4407, doi:10.1029/2002JD002670.

Risbey, J., M. Pook, P. McIntosh, M. Wheeler, and H. Hendon, 2009: On the remote drivers of rainfall variability in Australia. *Mon. Wea. Rev.,* **137,** 3233–3253, doi:10.1175/2009MWR2861.1.

Saji, N. H., and T. Yamagata, 2003: Possible impacts of Indian Ocean dipole mode events on global climate. *Climate Res.,* **25,** 151–169, doi:10.3354/cr025151.

——, B. N. Goswami, P. N. Vinayachandran, and T. Yamagata, 1999: A dipole mode in the tropical Indian Ocean. *Nature,* **401,** 360–363.

Seidel, D. J., Q. Fu, W. J. Randel, and T. J. Reichler, 2008: Widening of the tropical belt in a changing climate. *Nat. Geosci.,* **1,** 21–24, doi:10.1038/ngeo.2007.38.

Smith, I. N., P. McIntosh, T. J. Ansell, C. J. C. Reason, and K. L. McInnes, 2000: Southwest Western Australian winter rainfall and its association with Indian Ocean climate variability. *Int. J. Climatol.,* **20,** 1913–1930, doi:10.1002/1097-0088(200012)20:15<1913::AID-JOC594>3.0.CO;2-J.

Son, S., N. F. Tandon, L. M. Polvani, and D. W. Waugh, 2009: Ozone hole and Southern Hemisphere climate change. *Geophys. Res. Lett.,* **36,** L15705, doi:10.1029/2009GL038671.

Speer, M. S., L. M. Leslie, and A. O. Fierro, 2011: Australian east coast rainfall decline related to large scale climate drivers. *Climate Dyn.,* **36,** 1419–1429, doi:10.1007/s00382-009-0726-1.

Taylor, K. E., R. J. Stouffer, and G. A. Meehl, 2012: An overview of CMIP5 and the experimental design. *Bull. Amer. Meteor. Soc.,* **93,** 485–498, doi:10.1175/BAMS-D-11-00094.1.

Thompson, D. W. J., and S. Solomon, 2002: Interpretation of recent Southern Hemisphere climate change. *Science,* **296,** 895–899, doi:10.1126/science.1069270.

Timbal, B., and W. Drosdowsky, 2013: The relationship between the decline of southeastern Australian rainfall and the strengthening of the subtropical ridge. *Int. J. Climatol.,* **33,** 1021–1034, doi:10.1002/joc.3492.

Ummenhofer, C. C., A. Sen Gupta, M. J. Pook, and M. H. England, 2008: Anomalous rainfall over southwest Western Australia forced by Indian Ocean sea surface temperatures. *J. Climate,* **21,** 5113–5134, doi:10.1175/2008JCLI2227.1.

——, M. H. England, P. C. McIntosh, G. A. Meyers, M. J. Pook, J. S. Risbey, A. Sen Gupta, and A. S. Taschetto, 2009: What causes southeast Australia's worst droughts? *Geophys. Res. Lett.,* **36,** L04706, doi:10.1029/2008GL036801.

——, and Coauthors, 2011: Indian and Pacific Ocean influences on southeast Australian drought and soil moisture. *J. Climate,* **24,** 1313–1336, doi:10.1175/2010JCLI3475.1.

Verdon-Kidd, D. C., and A. S. Kiem, 2009: Nature and causes of protracted droughts in southeast Australia: Comparison between the Federation, WWII, and Big Dry droughts. *Geophys. Res. Lett.,* **36,** L22707, doi:10.1029/2009GL041067.

Wang, G., and W. Cai, 2013: Climate-change impact on the 20th-century relationship between the southern annular mode and global mean temperature. *Sci. Rep.,* **3,** 2039, doi:10.1038/srep02039.

Weller, E., and W. Cai, 2013: Realism of the Indian Ocean dipole in CMIP5 models: The implication for climate projections. *J. Climate,* **26,** 6649–6659, doi:10.1175/JCLI-D-12-00807.1.

Xie, S.-P., K. Hu, J. Hafner, H. Tokinaga, Y. Du, G. Huang, and T. Sampe, 2009: Indian Ocean capacitor effect on Indo–western Pacific climate during the summer following El Niño. *J. Climate,* **22,** 730–747, doi:10.1175/2008JCLI2544.1.

Zheng, X.-T., S.-P. Xie, Y. Du, L. Liu, G. Huang, and Q. Liu, 2013: Indian Ocean dipole response to global warming in the CMIP5 multimodel ensemble. *J. Climate,* **26,** 6067–6080, doi:10.1175/JCLI-D-12-00638.1.